

M giants with IGRINS

I. Stellar parameters and α -abundance trends of the solar neighborhood population

G. Nandakumar¹, N. Ryde¹, L. Casagrande^{2,3}, and G. Mace^{4,5}

¹ Lund Observatory, Division of Astrophysics, Department of Physics, Lund University, Box 43, SE-221 00 Lund, Sweden
e-mail: govind.nandakumar@fysik.lu.se

² Research School of Astronomy and Astrophysics, The Australian National University, Canberra, ACT 2611, Australia

³ ARC Centre of Excellence for All Sky Astrophysics in 3 Dimensions (ASTRO 3D), Australia

⁴ Department of Astronomy, The University of Texas, Austin, TX 78712, USA

⁵ McDonald Observatory, The University of Texas, Austin, TX 78712, USA

Received ; accepted

ABSTRACT

Context. Cool stars, such as M giants, can only be analysed in the near-infrared (NIR) regime due to the ubiquitous TiO features in optical spectra of stars with $T_{\text{eff}} < 4000$ K. In dust obscured regions, like the inner bulge and Galactic Center region, the intrinsically bright M giants observed in the near-infrared is an optimal option to study stellar abundances and the chemical evolution of stellar populations. Due to uncertainties in photometric methods, a method to determine the stellar parameters for M giants from the near-IR spectra themselves is needed.

Aims. To develop a method to determine the stellar parameters for M giants from the near-IR spectra. Validate the method by deriving the stellar parameters for nearby well-studied M-giants with spectra from the IGRINS spectral library. Demonstrate the accuracy and precision by determining stellar parameters and α -element trends versus metallicity for solar neighbourhood M giants.

Methods. We have carried out new observations of 44 M giant stars with IGRINS mounted on the Gemini South telescope within the programs GS-2020B-Q-305 and GS-2021A-Q302. We also obtained the full H and K band IGRINS spectra of six nearby well-studied M giants at a spectral resolving power of $R=45,000$ from the IGRINS spectral library. We use the Spectroscopy Made Easy (SME) tool in combination with one-dimensional (1D) Model Atmospheres in a Radiative and Convective Scheme (MARCS) stellar atmosphere models to model the synthetic spectrum that best fits the observed spectrum.

Results. The effective temperatures that we derive from our new method (here tested for $3400 \leq T_{\text{eff}} \leq 4000$ K) agree excellently with six nearby, well-studied M giants which indicates that the accuracy is indeed high. For the 43 solar neighborhood M giants, our T_{eff} , $\log g$, $[\text{Fe}/\text{H}]$, ξ_{micro} , $[\text{C}/\text{Fe}]$, $[\text{N}/\text{Fe}]$, and $[\text{O}/\text{Fe}]$ are in unison with APOGEE with mean differences and scatter (our method - APOGEE) of -67 ± 33 K, -0.31 ± 0.15 dex, 0.02 ± 0.05 dex, 0.22 ± 0.13 km/s, -0.05 ± 0.06 dex, 0.06 ± 0.06 dex, and 0.02 ± 0.09 dex, respectively. Furthermore, the tight offset with a small dispersion compared to APOGEE's T_{eff} points to a high precision in both our derived temperatures and those derived from the APOGEE pipeline. Typical uncertainties in the stellar parameters are found to be ± 100 K in T_{eff} , ± 0.2 dex in $\log g$, ± 0.1 dex in $[\text{Fe}/\text{H}]$, ± 0.1 km/s in ξ_{micro} . The α -element trends versus metallicity for Mg, Si, Ca and Ti are consistent with both APOGEE DR17 trends for the same stars as well as with the GILD optical trends. We also find clear enhancement in abundances for thick disc stars.

Key words. stars: abundances, late-type- Galaxy:evolution, disk- infrared: stars

1. Introduction

As necessary ingredients in any spectroscopic analyses and specifically in order to accurately estimate detailed elemental abundances from stellar spectra, the fundamental parameters of stars are crucial to determine. These are the effective temperature (T_{eff}), surface gravity ($\log g$), metallicity ($[\text{Fe}/\text{H}]$) and microturbulence (ξ_{micro} ; in the case of 1D stellar atmospheres). With the advent of bigger telescopes and major advancement in the instruments to efficiently record spectra in the visual or optical wavelength regime, there has been a huge progress in the spectroscopic analysis techniques to estimate accurate fundamental stellar parameters (see, e.g., Jofré et al. 2019). This has also led to advances in large-scale analyses of optical spectroscopic surveys like GALAH (Buder et al. 2021), LAMOST (He et al. 2017), Gaia-ESO (Randich et al. 2022) and several others which

observe and analyse the stellar spectra of millions of stars of different spectral types and at various evolutionary stages. Yet these surveys provide reliable stellar parameters and abundances mainly for the relatively warmer FGK type stars ($T_{\text{eff}} > 4000$ K; Jofré et al. 2019) since the optical spectra of the ubiquitous, cooler M-type stars are riddled by diatomic (e.g., TiO, FeH, OH, CO) and triatomic (e.g., H₂O) molecules in their atmospheres making their optical spectra nearly impossible to analyse.

Spectra of M-type stars in the near-infrared wavelength regime ($0.75 \mu\text{m} - 2.4 \mu\text{m}$) are, however, feasible to analyse. This opens up the possibility to use these stars in spectroscopic analyses and to use them as probes for the study of stellar populations. In addition, stars in direction of high extinction are preferably analysed in the infrared. For instance, spectroscopic investigations of stars in the heavily dust enshrouded Galactic Centre region demand observations at near-infrared wavelengths and also

limit the observable stellar populations to the relatively brighter M-giant stars. This calls for the development of spectroscopic techniques to determine reliable stellar parameters also from spectra recorded at the near-IR wavelengths. With the immense possibility of observing more distant M giants with the upcoming large telescopes like ELT (de Zeeuw et al. 2014) and TMT (Skidmore 2022) with the high-resolution, near-infrared spectroscopic instruments projected for them (Maiolino et al. 2013; Genoni et al. 2016; Mawet et al. 2019), there is an urgent need to develop methods to derive reliable stellar parameters from near infrared spectra of M giants.

Existing methods to determine the effective temperatures, T_{eff} , of M giants like those based on interferometry (Mozurkewich et al. 2003), the infrared flux method (IRFM; Casagrande 2008), and the color- T_{eff} relation (Bessell et al. 1998) are limited to nearby stars and also subjected to uncertainties arising due to interstellar reddening. Thus, the determination of T_{eff} using the above mentioned methods is less useful for the distant and heavily extinct stars in the inner Milky Way regions thus demanding methods that can extract stellar parameters directly from near-infrared spectra. Such methods for GK stars ($T_{\text{eff}} > 4000$ K) using the ratios of the depths between low- and high-excitation lines (i.e. line depth ratios; Gray 2008) have been attempted in recent studies (Fukue et al. 2015, Taniguchi et al. 2018, Taniguchi et al. 2021, Matsunaga et al. 2021, Afşar et al. 2023) but have been found to be affected by metallicity and abundance ratios (Jian et al. 2019). Ryde & Schultheis (2015) and Schultheis et al. (2016) determined T_{eff} for M giant stars in the Solar neighbourhood and the Galactic Centre by using the spectral indices of CO band heads in low-resolution K-band spectra and Thorsbro et al. (2018, 2020) used spectral indices of K band Scandium lines. Similarly, Ghosh et al. (2019, 2021, 2022) determined metallicity dependent T_{eff} -equivalent width relations using low resolution H- and K- band spectra of cool stars. But these methods need further refinement and tests using reliable benchmark stars.

Similarly asteroseismology, considered to be one of the reliable methods to determine the surface gravities, $\log g$, of giants, is currently tested only for warmer giants (Pinsonneault et al. 2018) and also needs high quality repeated observations. Another way is to use the fundamental relation of $\log g$ (Nissen et al. 1997) that demands reliable values of mass, luminosity, stellar radius and distance measurements:

$$\log \frac{g}{g_{\odot}} = \log \frac{M}{M_{\odot}} - 4 \log \frac{T_{\text{eff}}}{T_{\text{eff}_{\odot}}} + 0.4(M_{\text{bol}} - M_{\text{bol}_{\odot}}) \quad (1)$$

where M is the stellar mass, T_{eff} is the effective temperature and M_{bol} is the absolute bolometric magnitude estimated from the distance modulus relation. This again is possible only for bright nearby stars with reliable parallax measurements from astrometry mission like the Gaia mission (Gaia Collaboration et al. 2021). This necessitates the development of other methods to determine surface gravity from the near infrared spectra of distant M giants.

In this paper, we present an iterative method using Spectroscopy made easy (SME; Valenti & Piskunov 1996, 2012) to determine reliable stellar parameters of cool M giants ($3400 \lesssim T_{\text{eff}} \lesssim 4000$ K) in the solar neighbourhood from near-infrared, H-band spectra. We demonstrate the method by using IGRINS spectra at spectral resolving power of $R \sim 45,000$ and make use of T_{eff} sensitive molecular OH lines in combination with CO molecular bands and Fe lines. The details of the observations and data reduction procedure are described in the section 2. In section 3, we give a brief description of the line

list used in this work and in section 4 we describe our iterative method used to determine stellar parameters for six nearby well studied M giants based on spectra from the IGRINS spectral library (Park et al. 2018; Sawczynec et al. 2022) in section 5. We show the quality of our parameter estimates by comparing the determined T_{eff} with reliable values in literature (from interferometry, photometric and spectroscopic methods) and if available, $\log g$ and $[\text{Fe}/\text{H}]$. With this method, we then determine stellar parameters and α -element abundances of 44 solar neighbourhood M giants which are also observed by the near infrared spectroscopic survey, APOGEE (Apache Point Observatory Galactic Evolution Experiment; Holtzman et al. 2018; Jönsson et al. 2018). In section 5, we also compare stellar parameters and the α -element abundance trends with respect to APOGEE and other literature sources. Final conclusions are in the section 7.

2. Observations and Data Reduction

In this work, we have analysed near-infrared spectra of 50 M giants observed with the Immersion GRating Infrared Spectrograph (IGRINS; Yuk et al. 2010; Wang et al. 2010; Gully-Santiago et al. 2012; Moon et al. 2012; Park et al. 2014; Jeong et al. 2014). IGRINS provides spectra spanning the full H and K bands (1.45 - 2.5 μm) with a spectral resolving power of $R \sim 45,000$. We have carried out new observations of 44 M giant stars with IGRINS mounted on the Gemini South telescope (Mace et al. 2018) within the programs GS-2020B-Q-305 and GS-2021A-Q302. The observations were performed in Service Mode in Jan to April 2021. Details of the observations are listed in the Table 1. We also analyse the IGRINS spectra of six nearby M giants available in the IGRINS spectral library (Park et al. 2018; Sawczynec et al. 2022), which we present in Table 2.

The IGRINS observations were carried out in one or more ABBA nod sequences along the slit permitting sky background subtraction. The exposure times were set to aim at an average signal-to-noise ratios (SNR)¹ of at least 100, leading to observing times ranging from 5 to 25 minutes. In all cases apart from a few a SNR above 100 was achieved, see last column in Table 1. For a third of the observations two or three times the SNR was achieved due better than expected weather conditions.

We used the IGRINS PipeLine Package (IGRINS PLP; Lee et al. 2017) to optimally extract the telluric corrected, wavelength calibrated spectra after flat-field correction and A-B frame subtraction. The spectral orders of the science targets and the telluric standards are subsequently stitched together after normalizing every order and then combining them in iraf (Tody 1993), excluding the low signal-to-noise edges of every order. This resulted in one normalized stitched spectrum for the entire H and K bands. However, to take care of any modulations in the continuum levels of the spectra we put large attention in defining specific local continua around the spectral line being studied. This turns out to be an important measure for accurate determinations of the α element abundances, see for example Santos-Peral et al. (2020). In the subsequent abundance analysis we also allow for wavelength shifts in order to fit the lines in the line masks we will use. This will take care of any errors or trends in the wavelength solution.

The standard procedure for eliminating the contaminating telluric lines is to divide with a telluric standard-star spectrum,

¹ SNR is provided by RRISA (The Raw & Reduced IGRINS Spectral Archive; Sawczynec et al. 2022) and is the average SNR for the H or K band and is per resolution element. It varies over the orders and is lowest at the end of the orders

Table 1: Observational details of K giant stars.

Index	2MASS ID	H ₂ MASS (mag)	K ₂ MASS (mag)	Date UT	Exposure Time mm:ss	SNR _H (per resolution element)	SNR _K
1	2M05484106-0602007	7.0	6.7	2021-01-02	06:32	110	130
2	2M05594446-7212111	7.0	6.8	2021-01-02	10:35	100	120
3	2M06035110-7456029	7.0	6.7	2021-01-01	13:25	90	110
4	2M06035214-7255079	7.1	6.8	2021-01-01	06:04	100	110
5	2M06052796-0553384	7.0	6.6	2021-01-02	07:08	100	120
6	2M06074096-0530332	7.3	6.5	2021-01-02	08:22	90	130
7	2M06124201-0025095	7.0	6.7	2021-01-01	07:34	90	100
8	2M06140107-0641072	7.2	6.8	2021-01-02	06:02	50	65
9	2M06143705-0551064	7.2	6.9	2021-01-02	07:13	70	90
10	2M06171159-7259319	7.2	6.9	2021-01-02	06:21	120	130
11	2M06223443-0443153	7.1	6.8	2021-01-02	08:35	90	110
12	2M06231693-0530385	7.1	6.7	2021-01-02	08:05	80	100
13	2M06520463-0047080	7.1	6.7	2021-01-02	06:41	80	100
14	2M06551808-0148080	7.1	6.8	2021-01-02	04:10	90	100
15	2M06574070-1231239	7.3	6.9	2021-01-02	09:31	90	110
16	2M10430394-4605354	7.2	6.9	2021-02-11	06:22	120	120
17	2M11042542-7318068	7.2	6.9	2021-02-11	05:50	120	130
18	2M12101600-4936072	7.2	6.9	2021-02-19	06:28	70	90
19	2M13403516-5040261	7.1	6.8	2021-03-17	11:27	170	170
20	2M14131192-4849280	7.2	6.9	2021-03-17	09:02	150	150
21	2M14240039-6252516	6.6	6.2	2021-03-18	12:36	240	250
22	2M14241044-6218367	7.3	6.8	2021-04-17	09:38	230	260
23	2M14260433-6219024	7.2	6.8	2021-02-18	05:01	50	70
24	2M14261117-6240220	7.0	6.5	2021-02-14	08:09	80	100
25	2M14275833-6147534	7.0	6.5	2021-02-18	05:19	80	100
26	2M14283733-6257279	6.5	6.1	2021-02-18	06:59	70	90
27	2M14291063-6317181	7.4	6.9	2021-02-18	05:16	80	110
28	2M14311520-6145468	7.3	6.7	2021-04-20	06:32	150	170
29	2M14322072-6215506	6.7	6.4	2021-04-13	11:40	270	290
30	2M14332169-6302108	6.9	6.5	2021-04-20	05:45	120	130
31	2M14332869-6211255	6.5	6.1	2021-02-20	06:20	120	140
32	2M14333081-6221450	7.2	6.7	2021-03-18	10:10	210	240
33	2M14333688-6232028	7.2	6.8	2021-04-24	14:24	210	250
34	2M14345114-6225509	7.0	6.6	2021-04-24	13:55	270	300
35	2M14360142-6228561	6.4	6.0	2021-04-20	10:23	80	90
36	2M14360935-6309399	6.9	6.5	2021-04-20	06:40	90	100
37	2M14371958-6251344	6.7	6.3	2021-04-24	09:18	240	240
38	2M14375085-6237526	7.3	7.0	2021-04-20	07:49	100	120
39	2M15161949+0244516	7.2	7.0	2021-04-24	14:01	190	190
40	2M17584888-2351011	7.3	6.5	2021-04-28	08:21	200	290
41	2M18103303-1626220	7.3	6.5	2021-04-28	08:47	230	310
42	2M18142346-2136410	7.1	6.6	2021-04-28	12:19	240	280
43	2M18191551-1726223	7.2	6.6	2021-04-28	14:16	320	380
44	2M18522108-3022143	7.3	6.9	2021-04-28	24:03	320	320

showing only telluric lines and mostly no stellar features. In the IGRINS observing strategy, telluric stars were chosen to be rapidly rotating, late B to early A dwarfs, and observed close in time and at a similar air mass as the science targets. This procedure works very well for most wavelength regions. Apart from some broad Brackett lines of hydrogen², some spurious broadband spectral features might, however, turn up in the telluric standard-star spectrum. Special attention is given to lines in these regions.

In high-resolution spectra there might also appear broad absorption features due to Diffuse Interstellar Bands (DIBs, see, e.g., Geballe 2016). These are probably due to large molecules

in the Interstellar Medium (ISM) in the line-of-sight of the star in study. The DIBs are often weak and normally correlate with the reddening, $E_{(B-V)}$, thus mainly found in spectra of reddened stars. Most DIBs have been identified in optical spectra but some are found in the Near-IR (Geballe et al. 2011), and more are being identified with new instruments (e.g. with X-shooter, APOGEE, IGRINS, WINERED, and CRIRES in Cox et al. 2014; Elyajouri et al. 2017; Galazutdinov et al. 2017; Hamano et al. 2022; Ebenbichler et al. 2022, respectively). None of these known DIBs are close to the spectral lines that we use in the following discussion in this paper.

Finally, for the wavelength solutions, sky OH emission lines are used (Han et al. 2012; Oh et al. 2014) and the spectra are subsequently shifted to laboratory wavelengths in air after a stellar

² Brackett (n=7) line at 2166 nm

radial velocity correction. In addition, we make sure to carefully eliminate obvious cosmic-ray signatures in the spectra.

3. Analysis

In this work, spectral synthesis is carried out using the Spectroscopy Made Easy code (SME; Valenti & Piskunov 1996, 2012). SME generates synthetic spectra by calculating the spherical radiative transfer through a relevant stellar atmosphere model defined by its fundamental, stellar parameters. SME finds this model by interpolating in a grid of one-dimensional (1D) MARCS (Model Atmospheres in a Radiative and Convective Scheme) stellar atmosphere models (Gustafsson et al. 2008). These are hydrostatic model atmospheres in spherical geometry, computed assuming LTE, chemical equilibrium, homogeneity, and conservation of the total flux. In order to account for the non-LTE (NLTE) effects, we used a NLTE grid for which the departure coefficients were computed using the MPI-parallelised NLTE radiative transfer code Balder (Amarsi et al. 2018). The NLTE grids for Si, Mg, and Ca are from Amarsi et al. (2020) and for Fe from Lind et al. (2017) and Amarsi et al. (2016) (with subsequent updates Amarsi priv. comm.). SME applies departure coefficients by interpolating in these grids.

As a line list we used an updated version of the VALD linelist (Piskunov et al. 1995; Kupka et al. 2000; Ryabchikova et al. 2015) in this work. The transition probability (gf -values, i.e., product of statistical weight and oscillator strength) of the lines lacking reliable experimental gf -values have been determined astrophysically using the high resolution infrared solar flux spectrum of Wallace & Livingston (2003) and tested for Arcturus (α boo) using the high resolution ($R \sim 100,000$) infrared spectrum from the Arcturus atlas (Hinkle et al. 1995) and adopting the stellar parameters from Ramírez & Allende Prieto (2011). In the astrophysical determination of gf -values, we set the abundance of an element to a reference value (0.0 in the case of the Sun and from Ramírez & Allende Prieto 2011 for Arcturus) and fit a synthetic spectrum to the absorption line in the observed spectrum of the Sun or Arcturus by varying the gf -value.

For many lines, we adopted the broadening parameters (corresponding to the collisional broadening due to neutral hydrogen, and in some cases charged particles) from the ABO theory (Anstee & O'Mara 1991, 1995; Barklem & O'Mara 1997; Barklem et al. 1998) or from the spectral synthesis code BSYN based on routines from MARCS (Gustafsson et al. 2008). Details about the calculation of the broadening parameters for the magnesium multiplet lines in the K band can be found in Nieuwmunster et al. (2023).

A detailed validation of the linelist has been carried out using the IGRINS H and K band spectra of ~ 40 solar neighborhood K giants in the Giants in the Local disk (GILD) sample (Jönsson et al. in prep., which builds upon and improves the analysis described in Jönsson et al. (2017)). The stellar parameters and abundances for stars in the GILD sample are determined from optical FIES spectra. The linelist used in this work has been validated by comparing the elemental abundance trends determined from IGRINS near infrared absorption lines for the above mentioned K giants with the trends for the same stars determined in GILD with a reliable optical linelist (Nandakumar et al. in prep.). The linelist used in this work have been used in Montelius et al. 2022; Nandakumar et al. 2022; Nieuwmunster et al. 2023. Thus we use a linelist with carefully selected and reliable lines that have been tested not only with the Sun and the Arcturus but also with ~ 40 solar neighborhood K giants.

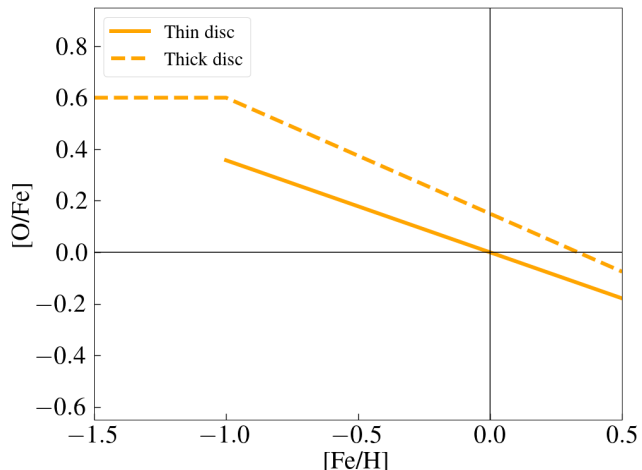


Fig. 1: A simple functional form of the $[O/Fe]$ versus $[Fe/H]$ trend for thin and thick disc stellar populations (or better 'low- α ' and 'high- α ' populations; see Minchev et al. 2017) adopted from Amarsi et al. (2019). In our parameter estimation method, we assumed $[O/Fe]$ values for our stars corresponding to a particular metallicity value depending on whether they belong to the thin or thick disc population.

The line data for the CO, CN, and OH molecular lines are adopted from the line lists of Li et al. (2015), Brooke et al. (2016) and Sneden et al. (2014), respectively. The central wavelengths and gf -values values of the selected OH, CN, and CO molecular lines used in the stellar parameter estimation method (see Section 4) are listed in the Tables A.3, A.4, and A.5, respectively. The central wavelengths, VALD or astrophysically calibrated gf -values and broadening parameters of Mg, Si, Ca, Ti and Fe are listed in the Table A.2.

4. Method

An accurate determination of the effective temperature, T_{eff} , is crucial in spectroscopic analyses, as T_{eff} defines the energy transported through a star thus shaping of the continuum of the stellar spectrum, the excitation balance of lines, and ionization stages of elements. Hence, we started by identifying T_{eff} -sensitive absorption lines in the H band regime that can be used to constrain T_{eff} . We chose a random set of 236 stars from the APOGEE DR17 catalog within 100 K bins between $3000 \text{ K} < T_{\text{eff}} < 4500 \text{ K}$, and 0.5 dex bins between $-1.5 < [Fe/H] < 0.5$ dex. Based on careful visual inspection of APOGEE spectra of stars with different T_{eff} but similar set of $\log g$, $[Fe/H]$, ξ_{micro} etc, we identified a set of ~ 50 molecular OH-lines that are sensitive to T_{eff} . We further selected a subset of 15 to 20 OH lines from which we were able to recover the APOGEE T_{eff} within $\pm 100 \text{ K}$ when we run SME with T_{eff} set as a free parameter for the 236 stars. In addition to T_{eff} , the strength of these lines are also dependent on the oxygen (O) abundance. Thus, it is necessary for this method that the O abundance be known or fixed in order to constrain the T_{eff} from OH lines.

Amarsi et al. (2019) derived 3D NLTE O abundances for 187 F and G dwarfs belonging to thin disc, thick disc and halo of the Milky Way. Based on their Figure 12 (left panel) we have made functional forms of the $[O/Fe]$ versus $[Fe/H]$ trend for thin and thick discs, as shown in Figure 1. We used these functional forms

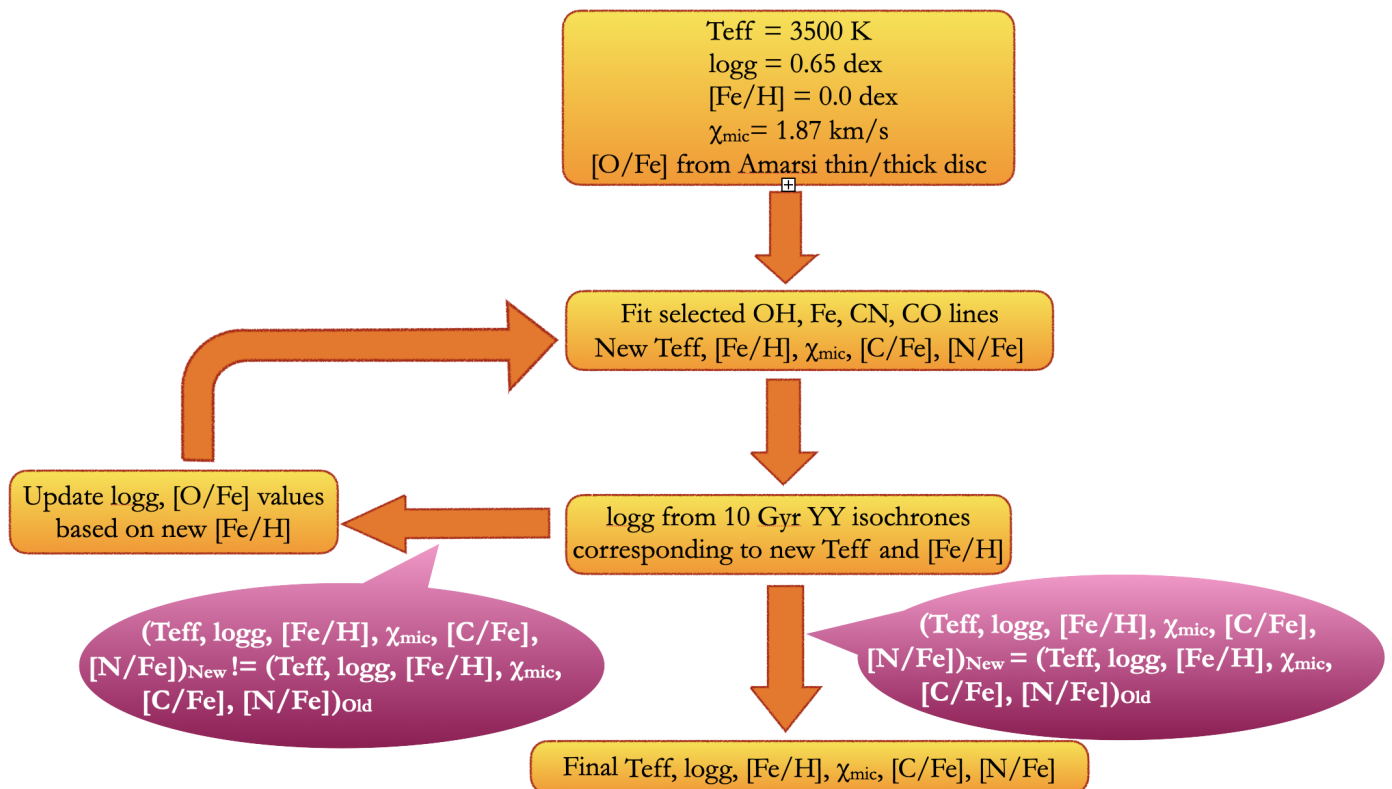


Fig. 2: Flow diagram of the method to determine reliable stellar parameters of cool M giants ($3400 \lesssim T_{\text{eff}} \lesssim 4000$ K) from near-infrared, H-band spectra.

of trends to fix $[O/Fe]$ for stars with any metallicity belonging to the thin or the thick disc³.

In addition to the OH lines, we have chosen a set of CN and CO lines (including molecular band heads) and Fe lines as listed in Tables A.4, A.5 and A.2 respectively. This will constrain the molecular equilibrium of C, N, and O bearing molecules, and the metallicity.

As the first assumption, we categorise the star into a thin disc or thick disc star. We then assume a starting T_{eff} and $[Fe/H]$ of 3500 K and 0.00 dex, respectively. For this T_{eff} and $[Fe/H]$ we get a $\log g$ of 0.65 for a 10 Gyr old star from the Yonsei-Yale isochrones by means of simple linear interpolation (see also Rich et al. 2017). At this metallicity, $[O/Fe]$ is 0.0 for a thin disc star and 0.15 for a thick disc star. In the initial step, we run SME setting T_{eff} , $[Fe/H]$, ξ_{micro} , C, and N abundances as free parameters for the selected set of lines. SME generates and fits multiple synthetic spectra for all the chosen lines of interest for different combinations of the free parameters. The final values of the parameters are determined from the model with the best fits of the chosen lines by means of χ^2 minimization between the synthesized spectrum and the observed one in the marked regions of the chosen spectral lines. This initial step results in a new set of T_{eff} and $[Fe/H]$, which can be used to constrain $\log g$ from the Yonsei-Yale (YY) isochrones assuming old ages of 3-10 Gyr (Demarque et al. 2004). In the next SME run, we use the T_{eff} , $[Fe/H]$, ξ_{micro} , C and N abundances from the previous run, $\log g$ from the YY isochrone tracks and $[O/Fe]$ at the new $[Fe/H]$ based on the trend in Figure 1. This cycle is repeated

until the difference between values of all free parameters from the current SME run and the previous SME run is negligible. In the Figure 2 we show the flow diagram indicating the sequence of steps followed in the method.

While T_{eff} and $[Fe/H]$ are mainly constrained by the OH lines and Fe lines respectively, different sets of weak and strong lines help constrain the ξ_{micro} . Inclusion of CO and CN lines not only constrain the C, N abundances but also results in excellent synthetic spectra fit to the observed CN, CO lines thus taking care of the CN, CO blends as well. At the same time, when we carry out the entire exercise excluding the CN, CO lines and thus removing C and N from the set of free parameters, there is negligible difference in all stellar parameter values except $[Fe/H]$ which is found to vary within 0.1 dex. This could be an indication of possible CN, and/or CO blends in the Fe lines we have selected.

5. Validation of the Method

In this section, we validate our method described in the previous section by determining stellar parameters for six nearby M giants (see Section 5.1.1) some of which have reliable parameters in the literature. We then use the method to determine stellar parameters for 44 solar neighborhood M giants (see Section 5.1.2) followed by a discussion on uncertainties (see Section 5.2). We later determine the α abundance trends from selected Mg, Si, Ca and Ti lines (Section 6) which further proves the usefulness of the method by showing the precision and accuracy of the abundance trends compared to those determined based on other methods.

³ It would actually be more correct to call these populations 'low α population' instead of a thin disc population and 'high α population' instead of a thick disc population (see, e.g., Minchev et al. 2017).

Table 2: The fundamental stellar parameters estimated from the IGRINS spectra of six benchmark stars using our method and the literature compilation of stellar parameters (indicated by the *lit* subscript). The literature references are listed in the footnote and are indicated by the corresponding number as superscript to the parameter value in the table. We have listed $\log g$ and $[\text{Fe}/\text{H}]$ values as ‘–’ if there are no $\log g$, $[\text{Fe}/\text{H}]$ measurements in the literature (for example, in case of optical interferometric measurements like in Baines et al. (2021) or T_{eff} versus $(V-K)_0$ relation in Bessell & Brett (1988))

Star	V	K_{2MASIS}	E(B-V)	T_{eff} (K)	$T_{\text{eff lit}}$ (K)	$\log g$ (dex)	$\log g_{\text{lit}}$ (dex)	$[\text{Fe}/\text{H}]$ (dex)	$[\text{Fe}/\text{H}]_{\text{lit}}$ (dex)
HD 132813	4.54	-0.96	0.02	3457	3410 ± 37^1	0.43	–	-0.27	–
					3406^2		0.53^2		–
					3387 ± 39^3		0.46 ± 0.25^3		-0.09 ± 0.18^3
					3458^4		–		–
HD 89758	3.05	-1.01	0.01	3807	3868 ± 37^1	1.15	–	-0.09	–
					3793 ± 50^5		1.07 ± 0.10^5		-0.34 ± 0.10^5
					3822 ± 43^3		1.39 ± 0.17^3		-0.20 ± 0.06^3
					3777^4		–		–
HD 175588	4.3	-1.25	0.11	3484	3394 ± 32^1	0.49	–	-0.04	–
					3408^2		–		–
					3484 ± 16^3		0.47 ± 0.17^3		-0.14 ± 0.16^3
					3487^4		–		–
HD 224935	4.41	-0.40	0.04	3529	3490 ± 35^1	0.64	–	-0.10	–
					3504^2		–		–
					3592^4		–		–
					–		–		–
HD 101153	5.36	-0.21	0.04	3438	3421 ± 35^3	0.51	0.48 ± 0.25^3	-0.07	-0.09 ± 0.12^3
					3418 ± 100^6		0.49 ± 0.25^6		0.00 ± 0.10^6
					3455^4		–		–
					–		–		–
HD 96360	8.09	2.77	0.02	3459	3432^2	0.5	–	-0.15	–
					3471 ± 22^3		0.8 ± 0.23^3		0.0 ± 0.17^3
					$3550 \pm 100^{6,7}$		$0.72 \pm 0.25^{6,7}$		$-0.37 \pm 0.10^{6,7}$
					3484^4		–		–

Notes.

1: Baines et al. (2021), 2: Lebzelter et al. (2019), 3: Sharma et al. (2016), 4: T_{eff} from Bessell et al. (1998) V-K relation, 5: Jönsson et al. (2014), 6: Guerço et al. (2019), 7: Smith & Lambert (1990)

5.1. Stellar parameters

5.1.1. Nearby M giants

As a test case of our method, we selected six nearby M giants, the H- and K-band spectra of which are available in the IGRINS spectral library (Park et al. 2018; Sawczynec et al. 2022). We compiled their T_{eff} , $\log g$, and $[\text{Fe}/\text{H}]$, derived using different methods from various literature sources. T_{eff} for four of these stars (HD 132813, HD 89758, HD 175588, and HD 224935) were estimated based on the very precise angular diameter measurements using the Navy Precision Optical Interferometer (NPOI) in combination with distances from Gaia parallaxes (Baines et al. 2021). Hence these values of T_{eff} are very accurate and reliable. Further, we also have T_{eff} for the four stars (HD 132813, HD 175588, HD 224935, and HD 96360) from Lebzelter et al. (2019), estimated using the $T_{\text{eff}}-(V-K)$ relation derived from a homogeneous set of angular diameters by Richichi et al. (1999). They also estimated $\log g$ for one star (HD 132813) using the fundamental relation of $\log g$ assuming a mass of 1.2 M_{\odot} , and luminosity and distances from Gaia. Unlike the above mentioned studies, Sharma et al. (2016) provides all three stellar parameters for five stars (HD 132813, HD 89758, HD 175588, HD 101153, and HD 96360) based on full spectrum fitting of 331 stars in the MILES and ELODIE spectral libraries making use of the newer version, V2, of the MILES interpolator and the spectrum fitting tool, ULySS. For one star (HD 89758), we found

all three stellar parameters in Jönsson et al. (2014) with the T_{eff} provided from angular diameter measurement by Mozurkewich et al. (2003), $\log g$ estimated using the fundamental relation, and $[\text{Fe}/\text{H}]$ determined from Fe I lines in a visual spectrum from the ELODIE spectral archive. For HD96360, Smith & Lambert (1990) estimated T_{eff} based on the T_{eff} -spectral-type relation from Tsuji (1981), $\log g$ using the fundamental relation assuming a mass of 1.5 M_{\odot} , and $[\text{Fe}/\text{H}]$ as the mean of the Ti, Fe and Ni abundances. These parameters were adopted by Guerço et al. (2019), who also provide all three stellar parameters for HD 101153 with, in this case, the T_{eff} estimated using the $T_{\text{eff}}-(V-K)_0$ relation from Bessell et al. (1998), $\log g$ using the PARAM 1.3 code, and $[\text{Fe}/\text{H}]$ determined using a sample of 19 Fe I lines in the K-band wavelength regime. Finally, for all six stars, we determined T_{eff} using the following $T_{\text{eff}}-(V-K)_0$ relation from Bessell et al. (1998):

$$T_{\text{eff}} = 9102.523 - 3030.654(V - K)_0 + 633.3732(V - K)_0^2 - 60.73879(V - K)_0^3 + 2.135847(V - K)_0^4 \quad (2)$$

By using the python package `dustmaps`⁴ we estimated the dereddened values of V and K for this equation, with the reddening values (E(B-V)) from the two dimensional map of dust,

⁴ <https://dustmaps.readthedocs.io/en/latest/>

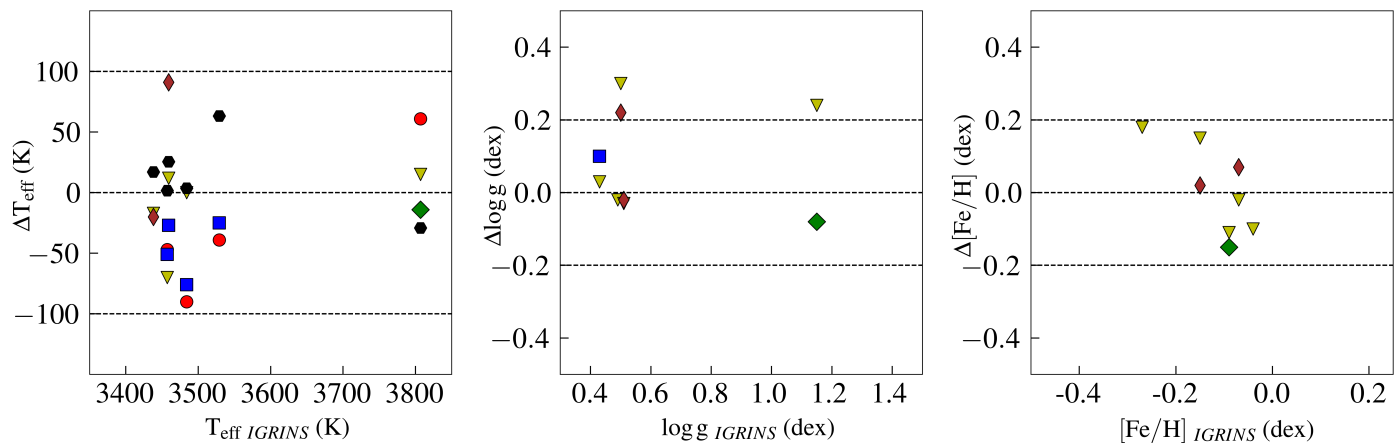


Fig. 3: The difference (literature - this work) in T_{eff} (left panel), $\log g$ (middle panel), and $[\text{Fe}/\text{H}]$ (right panel) on the y-axis versus the respective parameter estimates using our method (x-axis) for the six nearby M giant stars in the IGRINS spectral library. Different colored symbols represent the compiled literature estimates: red circles - Baines et al. (2021), blue squares - Lebzelter et al. (2019), green diamonds - Jönsson et al. (2014), yellow inverted triangles - Sharma et al. (2016), brown diamonds - Guerço et al. (2019). The black circles denote the T_{eff} estimated using the T_{eff} versus $(V-K)_0$ relation in Equation 2 (from Bessell et al. 1998). $K_{2\text{MAS}}S$ has been corrected to the photometric system in Bessell & Brett (1988) (https://irsa.ipac.caltech.edu/data/2MASS/docs/releases/allsky/doc/sec6_4b.html)

constructed by (Schlegel et al. 1998) based on far-infrared emission of dust. We use the conversion factors of 3.07 and 0.366 to determine the extinctions A_V and A_K respectively (see Table A1 in Casagrande & Vandenberg (2014)).

We also determined the stellar parameters for these stars with our method using IGRINS H-band spectra and assuming that the stars belong to the thin disc stellar population. Table 2 lists the stellar parameters for all six stars determined with our method along with the V , $K_{2\text{MAS}}S$ and $E(B-V)$ values, as well as the stellar parameters from the literature. In the Figure 3, we plot the difference in stellar parameters (literature - IGRINS) as a function of our IGRINS parameters. The differences in T_{eff} for comparisons with multiple literature sources, lie well within ± 100 K, with a minimum difference seen when compared to T_{eff} derived using the Bessell et al. (1998) relation for all six stars. The differences in $\log g$ are largest for HD96360 and HD89758 when compared to the values from Sharma et al. (2016) with uncertainties ~ 0.2 dex. We would like to point out that the rest of the stars with available $\log g$ have small differences that lie within 0.1 dex. The differences in $[\text{Fe}/\text{H}]$ also lie within levels of ± 0.2 dex which is also comparable to the uncertainties in the measurements in the literature. Thus overall, there is a very good agreement for all three stellar parameters we determined using our method for the six well studied nearby M giants. This clearly is an indication of the efficiency of our method to determine accurate stellar parameters for M giants.

5.1.2. Solar neighbourhood M giants

Next, we applied our method to our new IGRINS spectra of the 44 solar neighbourhood M giants. All 44 stars have also been observed by the APOGEE survey with their stellar parameters and individual elemental abundances available in the latest data release, DR17, for all stars except one (#39). We identified five stars belonging to the thick disc population based on their enhanced APOGEE magnesium abundance from the $[\text{Mg}/\text{Fe}]$ versus $[\text{Fe}/\text{H}]$ plot. Thus, we fixed the oxygen abundance for these five stars according to the thick-disc trend and for the remaining 40 stars according to the thin-disc trend in Figure 1. Later, based

on our abundance analysis (alpha abundances), #39 was identified to be a thick-disc star. When we re-estimated the parameters assuming the thick-disc oxygen trend (increase of 0.17 dex in $[\text{O}/\text{Fe}]$), we found a 110 K increase in T_{eff} , 0.23 dex increase in $\log g$, 0.07 dex decrease in $[\text{Fe}/\text{H}]$, 0.2 km/s increase in ξ_{micro} , 0.14 dex increase in $[\text{C}/\text{Fe}]$, and a 0.07 dex increase in $[\text{N}/\text{Fe}]$. It is surprising, and reassuring, that even after the initial misidentification, we were able to rightly deduce the correct population based on the abundances we derived using the wrong stellar parameters. Nevertheless, it is an encouraging sign that there are ways to identify and correct such wrong initial assumptions, see further discussion in the section on uncertainties, Section 5.2.

APOGEE derived T_{eff} , $\log g$, $[\text{Fe}/\text{H}]$, ξ_{micro} , ξ_{macro} , $[\text{C}/\text{M}]$, $[\text{N}/\text{M}]$, $[\text{O}/\text{M}]$, and general alpha abundance, $[\alpha/\text{M}]$, simultaneously using the APOGEE Stellar Parameter and Chemical Abundance Pipeline (ASPCAP; García Pérez et al. (2016)) by interpolating in a pre-computed grid of synthetic spectra and finding the best-fitting stellar parameters that describe an observed spectrum. In addition to the raw, spectroscopic parameters and abundances, APOGEE also provides calibrated values. Since the uncalibrated spectroscopic parameters and abundances are directly derived from the APOGEE spectra, in this work, we make use of spectroscopic parameters (reported under the ASPCAP output array FPARAM) to compare with the values we derived using our method.

In figure 4, we plot the difference in the parameters and abundances (our method - APOGEE) as a function of APOGEE uncalibrated values. We estimated the mean value of the differences and scatter (mid value of 84th and 16th percentiles) which are listed in each panel. The T_{eff} , estimated using our method is lower than APOGEE's T_{eff} , for all stars except two: #10 and #44. In general, the difference in T_{eff} is small with a mean of -67 K and scatter of 33 K, thus lying within 100 K for the majority of the stars with no significant trends. Similar to T_{eff} , the surface gravity, $\log g$, from our method is lower compared to APOGEE with a mean difference of -0.31 dex and scatter of 0.15 dex. We also see a trend of lower differences (< -0.1 dex) at lower values of APOGEE $\log g$ that increases to ~ -0.5 dex with larger scatter at higher values of APOGEE $\log g$. It has been pointed

This work - APOGEE spectroscopic estimates

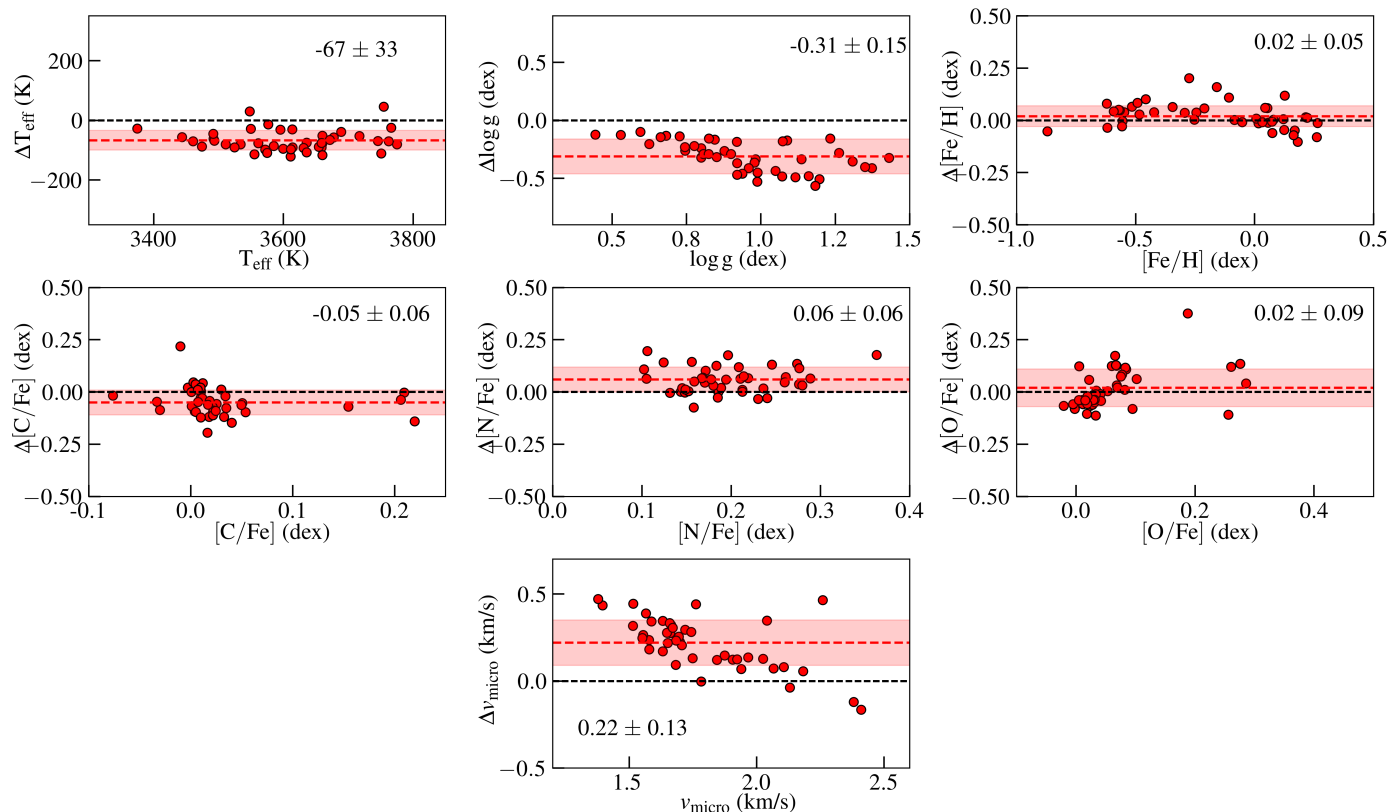


Fig. 4: The differences (this work - APOGEE spectroscopic estimates) in T_{eff} , $\log g$, $[\text{Fe}/\text{H}]$, ξ_{micro} , $[\text{C}/\text{Fe}]$, $[\text{N}/\text{Fe}]$, and $[\text{O}/\text{Fe}]$ on the y-axis versus the APOGEE spectroscopic estimates on the x-axis for the 44 stars in the solar neighborhood from our new IGRINS observations. T_{eff} , $\log g$, and $[\text{Fe}/\text{H}]$ are shown in the three panels in the top row, $[\text{C}/\text{Fe}]$, $[\text{N}/\text{Fe}]$, and $[\text{O}/\text{Fe}]$ in the three panels in the middle row, and ξ_{micro} in the bottom row panel. The black dashed line indicates difference value of 0.0 between APOGEE and our estimates. The mean difference and standard deviation (calculated as the mid value of 84th - 16th percentile values for each parameter) is indicated by the red dashed line and the red band respectively, and is also listed in the respective panels.

out in Holtzman et al. (2018) that the spectroscopic (raw) $\log g$ values for giants determined by APOGEE ASPCAP are systematically higher than those derived from asteroseismology. This could possibly explain the consistently lower difference we find in $\log g$. At the same time, currently available measurements of asteroseismic $\log g$ are limited to stars with $T_{\text{eff}} > 3800$ K (Pinsonneault et al. 2018). Our metallicities are in agreement with APOGEE metallicities with a mean difference of 0.02 dex and a small scatter of 0.05 dex. There is a hint of change in the trend in the metallicity differences, from positive to negative, at higher metallicities, but this cannot be confirmed with the current sample. The difference in ξ_{micro} shows a clear trend, with higher values using our method for lower APOGEE ξ_{micro} but tends to agree at higher APOGEE ξ_{micro} . Our ξ_{micro} for a majority of the stars lie in a narrow range of 1.8-2.4 km/s and a high value of 2.7 km/s for the most metal poor star, #10. It is encouraging that our values of ξ_{micro} are in reasonable range of values usually accepted for giants (Smith et al. 2013). Finally, on average we find small differences for $[\text{C}/\text{Fe}]$, $[\text{N}/\text{Fe}]$ and $[\text{O}/\text{Fe}]$ with respect to APOGEE. We note that $[\text{C}/\text{Fe}]$ from our method are higher for the five thick disc stars similar to what APOGEE finds.

On further cross match carried out with other large spectroscopic surveys, we found seven stars in the RAVE survey catalog (DR6; Steinmetz et al. (2020)) and four stars in the GALAH survey catalog (DR3; Buder et al. (2021)). Based on the quality flags, `algo_conv_madera` (set to 3) in RAVE and `flag_sp` (not set

to 0) in GALAH, these stars do not have reliable stellar parameters determined from their spectra in both the survey catalogs. Meanwhile, the photometric T_{eff} has been estimated using the IRFM method (Casagrande et al. 2010) for all five stars in RAVE and for one star in GALAH (Casagrande et al. 2021).

In addition to comparing against APOGEE's values, we estimated photometric effective temperatures using the $T_{\text{eff}}\text{-(V-K)}$ relation (Equation 2). In doing so, we explored the effect of different reddening values. For 11 stars we had $E(\text{B-V})$ from APOGEE directly (set 1, hexagons in Fig 5), whereas for 21 stars (set 2, crosses in Fig 5) we adopted reddening values from Schlegel et al. (1998) renormalized as described in Casagrande et al. (2019). The input photometry being the same, this comparison is a sobering example of how reddening alone can easily introduce a scatter of order ± 50 K for our sample.

In addition to using the above colour relation, we also implemented Gaia DR3 and 2MASS photometry in the IRFM as per Casagrande et al. (2021) adopting our spectroscopic values of $\log g$ and $[\text{Fe}/\text{H}]$ and our renormalized reddening values. To better gauge into the uncertainties, for each star we MonteCarlo the errors into the IRFM, adopting quoted uncertainties for input stellar parameters and photometry, and allowing for 10 percent uncertainty in reddening. For stars with $E(\text{B-V}) < 0.85$, our MonteCarlo uncertainties are within 100 K, but they linearly increase to several hundreds of K for higher values of reddening. In order to retain stars with reliably determined IRFM temperatures

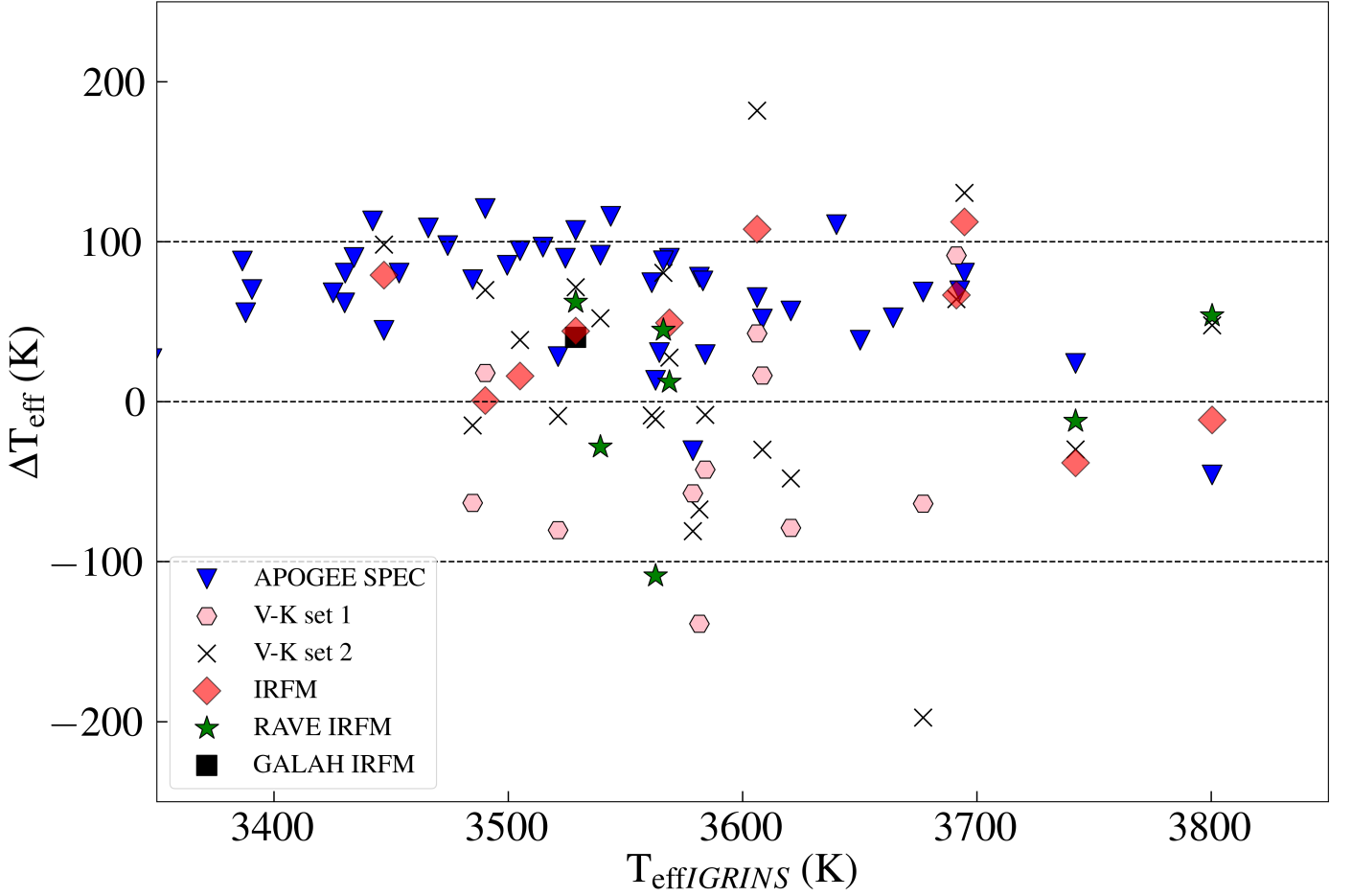


Fig. 5: The differences (GALAH/RAVE/APOGEE/(V-K)/IRFM - our method) in T_{eff} as a function of the T_{eff} derived using our method on the x-axis. The black dashed lines indicate the difference values of -100 K, 0 K and +100 K. Different colored symbols represent values from different sources: blue inverted triangles - APOGEE spectroscopic estimates, black squared - GALAH IRFM estimates, green star symbols - RAVE IRFM estimates, red diamonds - our IRFM T_{eff} estimates, and pink hexagons - T_{eff} estimated using T_{eff} versus (V-K) relation from Bessell et al. (1998) with extinctions in V and K based on the E(B-V) values from APOGEE.

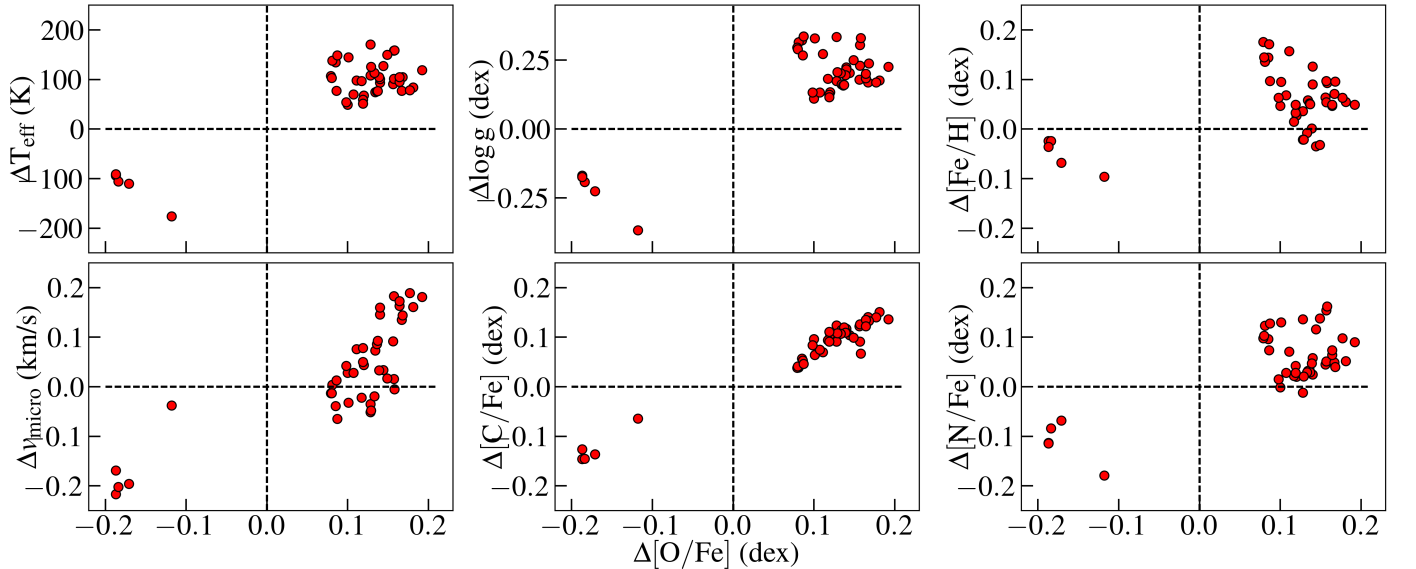


Fig. 6: The difference in T_{eff} , $\log g$, $[\text{Fe}/\text{H}]$, ξ_{micro} , $[\text{C}/\text{Fe}]$, and $[\text{N}/\text{Fe}]$ as a function of the difference in $[\text{O}/\text{Fe}]$ resulting from the change of population assumption from thin to thick disc and vice versa for the 44 solar neighborhood M giants. Circle markers with positive $\delta[\text{O}/\text{Fe}]$ values represent actual thin disc stars that are assumed to be thick disc for this exercise.

Table 3: Stellar parameters, [C/Fe] and [N/Fe] values of each star determined in this work along with their assumed stellar population and [O/Fe] based on the APOGEE [Mg/Fe] versus [Fe/H] trend.

Index	Population	T_{eff}	$\log g$	[Fe/H]	ξ_{micro}	[C/Fe]	[N/Fe]	[O/Fe]	Cross match
		K	$\log(\text{cm/s}^2)$	dex	km/s	dex	dex	dex	
1	thin	3490	0.48	-0.28	2.03	-0.02	0.17	0.1	–
2	thin	3694	0.74	-0.45	1.88	0.02	0.19	0.16	–
3	thick	3562	0.48	-0.51	2.14	0.21	0.3	0.38	RAVE
4	thick	3742	1.08	0.0	1.78	0.08	0.29	0.15	RAVE
5	thin	3677	0.92	-0.07	1.78	-0.12	0.21	0.04	–
6	thin	3692	0.68	-0.54	2.01	0.02	0.31	0.19	–
7	thin	3583	0.42	-0.66	2.39	0.05	0.33	0.24	–
8	thick	3620	0.65	-0.38	2.1	0.17	0.22	0.33	–
9	thin	3608	0.55	-0.52	2.24	0.06	0.27	0.19	–
10	thick	3800	0.59	-0.92	2.72	0.21	0.37	0.56	RAVE
11	thin	3521	0.4	-0.52	2.19	0.0	0.31	0.18	–
12	thin	3484	0.32	-0.55	2.09	0.04	0.3	0.2	–
13	thin	3581	0.67	-0.21	2.15	-0.09	0.31	0.08	–
14	thin	3606	0.52	-0.56	1.96	0.04	0.27	0.2	–
15	thin	3561	0.56	-0.36	2.24	-0.08	0.41	0.13	–
16	thin	3568	0.96	0.25	1.83	-0.18	0.39	-0.08	RAVE, GALAH*
17	thin	3566	0.51	-0.46	2.02	0.01	0.24	0.16	RAVE
18	thin	3539	0.5	-0.41	2.05	0.03	0.23	0.15	RAVE, GALAH*
19	thin	3528	0.61	-0.15	1.92	-0.02	0.13	0.06	RAVE, GALAH
20	thin	3504	0.61	-0.08	1.81	0.01	0.16	0.03	–
21	thin	3474	0.69	0.12	1.94	-0.07	0.21	-0.04	–
22	thin	3543	0.8	0.11	1.95	-0.05	0.2	-0.04	–
23	thin	3386	0.55	0.13	1.82	-0.04	0.14	-0.05	–
24	thin	3387	0.52	0.08	1.92	-0.03	0.21	-0.03	–
25	thin	3453	0.63	0.08	1.91	-0.1	0.22	-0.03	–
26	thin	3465	0.62	0.04	1.83	-0.09	0.33	-0.02	–
27	thin	3430	0.54	0.0	1.95	-0.02	0.16	-0.0	–
28	thin	3499	0.62	-0.06	2.01	-0.07	0.25	0.02	–
29	thin	3639	0.89	-0.0	1.76	-0.05	0.08	0.01	–
30	thin	3524	0.56	-0.25	1.98	0.02	0.15	0.09	–
31	thin	3664	1.11	0.23	1.99	-0.09	0.35	-0.08	–
32	thin	3430	0.55	0.02	1.92	-0.09	0.21	-0.01	–
33	thin	3425	0.54	0.02	1.87	-0.07	0.25	-0.01	–
34	thin	3442	0.68	0.18	1.85	-0.0	0.16	-0.06	–
35	thin	3514	0.53	-0.26	2.02	-0.04	0.16	0.09	–
36	thin	3446	0.61	0.08	1.99	-0.04	0.21	-0.03	–
37	thin	3650	0.98	0.1	1.8	-0.11	0.29	-0.04	–
38	thin	3582	0.96	0.23	1.8	-0.11	0.31	-0.09	–
39	thick	3691	0.76	-0.4	1.98	0.17	0.14	0.34	–
40	thin	3564	0.95	0.25	2.2	-0.04	0.38	-0.09	–
41	thin	3347	0.46	0.09	1.98	-0.09	0.21	-0.03	–
42	thin	3390	0.48	0.01	1.96	-0.01	0.27	-0.0	–
43	thin	3434	0.59	0.07	1.93	-0.07	0.24	-0.02	–
44	thick	3578	0.45	-0.59	2.26	0.08	0.54	0.41	GALAH*

Notes.*: No IRFM T_{eff} in GALAH DR3

we thus restrict ourselves to stars with $E(B-V)$ below the above threshold, which correspond to T_{eff} uncertainties in the range 30 to 60 K. From Figure 5 it is clear that the IRFM values (red diamonds) are consistent with our spectroscopic determinations, the mean difference being 42 K with a standard deviation of 48 K. We could not estimate IRFM temperatures for the six nearby M giants owing to their extreme brightness.

Figure 5 also shows the comparison with the IRFM effective temperatures from RAVE DR6 (Steinmetz et al. 2020). In this version of the IRFM APASS photometry was used instead,

along with $\log g$ and [Fe/H] derived from RAVE. This comparison shows the effect of the adopted stellar parameters and photometry, with the caveat that Gaia DR3 is far superior than APASS. Finally we also show the comparison with one stars with IRFM effective temperature from GALAH which was based instead on the Gaia DR2 photometry and transmission curves.

From the different values and methods compared in Figure 5 we can thus conclude that our effective temperature determinations are reliable especially in comparison with several other ones available in the literature. In particular, the scatter with re-

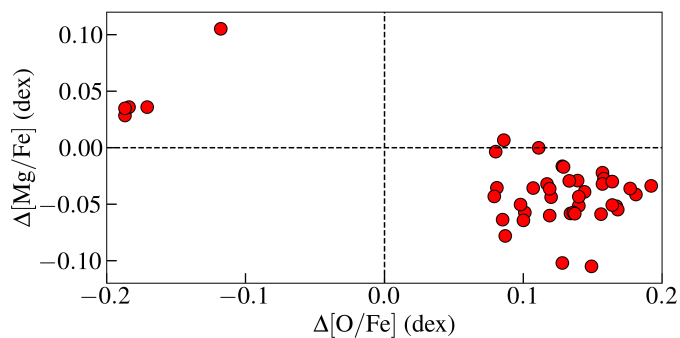


Fig. 7: Same as Figure 6 except for the difference in $[Mg/Fe]$ plotted on y-axis. It is evident that $[Mg/Fe]$ decreases for thin disc stars wrongly assumed to be thick disc and $[Mg/Fe]$ increases for thick disc stars wrongly assumed to be thin disc. This demonstrates that a wrong classification would be caught in the derived alpha abundances, and a corrective iteration of our method can be done.

spect to several photometric determinations points to the uncertainty introduced by the limited precision to which reddening can be estimated. Since our determined effective temperatures agree excellently with the six nearby, well studied M giants in the IGRINS spectral library (in Fig. 3), we have good reasons to believe that our values are more accurate. Especially, the moderately tight offset against T_{eff} from APOGEE points to good internal precision once a systematic offset of about 100 K for stars cooler than 3700 K is removed.

5.2. Uncertainties in the derived stellar parameters

As explained in the section 4, our method to estimate stellar parameters depends largely on the oxygen abundance which we fix based on the metallicity of the star and the Milky Way population to which the star belongs (see Figure 1). Thus, the assumption of the population or the oxygen abundance may be considered as the main source of uncertainty for our stellar parameters. Hence, in order to estimate typical uncertainties in the parameters and abundances we derive, we implemented our method assuming the 38 thin disc stars in the solar neighbourhood sample as thick disc stars and vice versa for the 6 thick disc stars. This is similar to the mis-classification of the star #39 as thin disc star in the section 5.1.2.

The results of this exercise are shown in the Figure 6 with the differences in oxygen abundance on the x-axis and the differences in six other stellar parameters on the y-axis in each panel. In this figure, actual thick disc stars have negative $\Delta[O/Fe]$, since $[O/Fe]$ is lower for the thin disc trend and the actual thin disc stars have positive $\Delta[O/Fe]$. Assuming lower oxygen abundance for the most metal poor star, #10, resulted in stellar parameters that were outside our adopted grid limits. Hence, we omit this star in this exercise. For the maximum difference of ± 0.2 dex in $[O/Fe]$, we found typical differences of ± 200 K in T_{eff} , ± 0.25 dex in $\log g$, ± 0.2 km/s in ξ_{micro} , ± 0.2 dex in $[C/Fe]$, and ± 0.2 dex in $[N/Fe]$. The difference in metallicity is found to be closer to 0 for $[O/Fe]$ differences of $+0.2$ and -0.2 dex, but larger (up to $\sim +0.2$ dex) in the range $0.0 < \Delta[O/Fe] < 0.2$ dex. Thus, assuming a typical uncertainty of 0.15 dex in $[O/Fe]$, the parameters estimated using our method will have typical uncertainties of ± 100 K in T_{eff} , ± 0.2 dex in $\log g$, ± 0.1 dex in $[Fe/H]$, ± 0.1 km/s in ξ_{micro} , ± 0.1 dex in $[C/Fe]$, and ± 0.1 dex in $[N/Fe]$. But again, as

we demonstrated for the star #39 in the section 5.1.2, a wrong classification would be caught in the derived alpha abundances, and a corrective iteration can be done. To make sure this was not a chance occurrence, we determined $[Mg/Fe]$ for all stars using stellar parameters determined based on a mis-classification. We found that the $[Mg/Fe]$ abundances decreases further for the wrongly classified thin disc star and increases further for the wrongly classified thick disc star. This is demonstrated in the Figure 7. We will, therefore, safely be able to catch any mis-classification of a high- or low-alpha star by inspecting the derived $[Mg/Fe]$ ratio.

Another source of uncertainty is the use of 10 Gyr YY isochrone to constrain $\log g$. As discussed in Rich et al. (2017), different age tracks for giants overlap which in turn should result in negligible difference in $\log g$ if we choose a lower age isochrone track. Indeed, we find that $\log g$ increases by only ~ 0.1 dex if we use a 2 Gyr YY isochrone instead of the 10 Gyr one.

Thus, we estimate the uncertainties in the derived stellar parameters using our method to be ± 100 K in T_{eff} , ± 0.2 dex in $\log g$, ± 0.1 dex in $[Fe/H]$, and ± 0.1 km/s in ξ_{micro} . Within these uncertainties, our parameters are in line with the comparison samples and methods presented in Figures 3-5.

6. α Abundance Trends

Based on the stellar parameters determined using our iterative method, we determined elemental abundances of the following α elements: Mg, Si, Ca and Ti, for the six nearby M giants and 44 solar neighbourhood M giants. We adopt the solar abundance values for Mg ($A(\text{Mg})_{\odot} = 7.53$), Si ($A(\text{Si})_{\odot} = 7.51$), Ca ($A(\text{Ca})_{\odot} = 6.31$) and Ti ($A(\text{Ti})_{\odot} = 4.90$) from Grevesse et al. (2007). In the following subsections, we discuss the individual and mean elemental abundance trends determined from a selected set of carefully selected absorption lines of each element in the H and K bands. For each element, we fitted the selected lines individually and determined the mean abundance value after removing lines that were too noisy, affected by spurious features, or affected by telluric lines that were not eliminated well enough in the telluric line removal procedure. From these chosen sets of abundances, we determined the mean abundance and a line-by-line scatter of each element for every star, see Tables A.6 to A.9. We will also compare the mean elemental abundance trends to the optical solar neighbourhood trends from *Giants In the Local Disk (GILD)* sample and to the APOGEE DR17 spectroscopic values if available. This comparison also serves as a way to further validate our stellar parameters and hence our method used to determine them.

In addition to the line-by-line scatter reported in the Tables A.6 to A.9, we determined the uncertainties in the elemental abundance estimates from each line that arise from the uncertainties in stellar parameters. As mentioned in Section 5.2, parameters estimated using our method will have typical uncertainties of ± 100 K in T_{eff} , ± 0.2 dex in $\log g$, ± 0.1 dex in $[Fe/H]$, ± 0.1 km/s in ξ_{micro} . We selected seven stars with metallicities of ~ -0.9 dex (#10), -0.5 dex (#11 and #44), -0.25 dex (#30), 0.0 dex (#29), 0.1 dex (#41) and 0.25 dex (#40) to determine uncertainties. Thus we cover the entire metallicity range explored in this study. We randomly generated 50 sets of stellar parameters following a normal distribution with the stellar parameter value as the mean and these typical uncertainties as the standard deviation, and reanalyse each stellar spectrum using those parameters. We generated 50 sets of parameters for each of the seven stars. The resulting distribution of estimated abundances

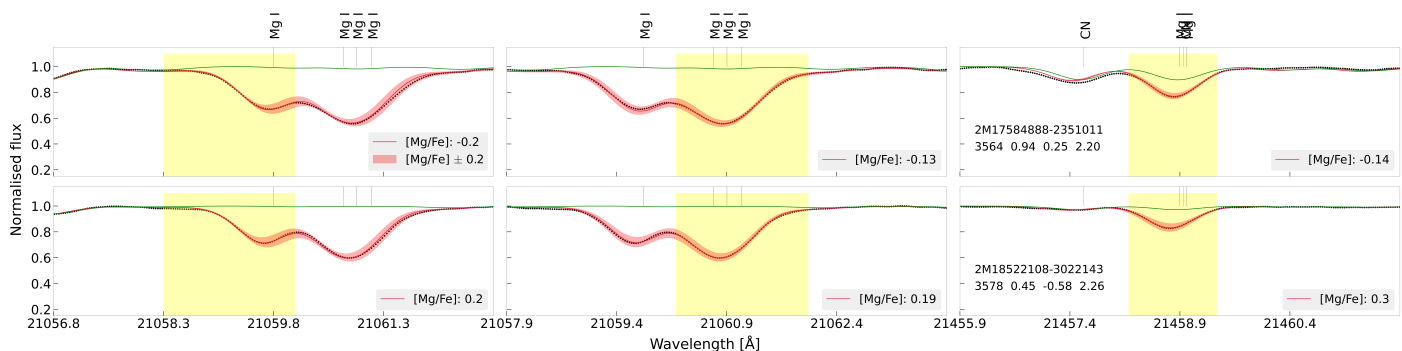


Fig. 8: Wavelength regions centered at the five selected Magnesium lines for the thin disc star 2M17584888-2351011 (#40; top row panels) and the thick disc star 2M18522108-3022143 (#44; bottom row panels) with the panels in each row arranged in the increasing order of wavelengths of selected lines. In each panel, the black circles denote the observed spectrum, crimson line denote the best fit synthetic spectrum and the red band denote the variation in the synthetic spectrum for ± 0.2 dex difference in the $[\text{Mg}/\text{Fe}]$. The yellow bands in each panel represent the line masks defined for the Mg lines wherein SME fits observed spectra by varying Magnesium abundance and finds the best synthetic spectra fit by chi-square minimisation. The green line shows the synthetic spectrum without Mg, also indicating any possible blends in the line. The $[\text{Mg}/\text{Fe}]$ values corresponding to the best fit case for each Mg line is listed in each panel. All identified atomic and molecular lines are also denoted in the top part of the top row panels.

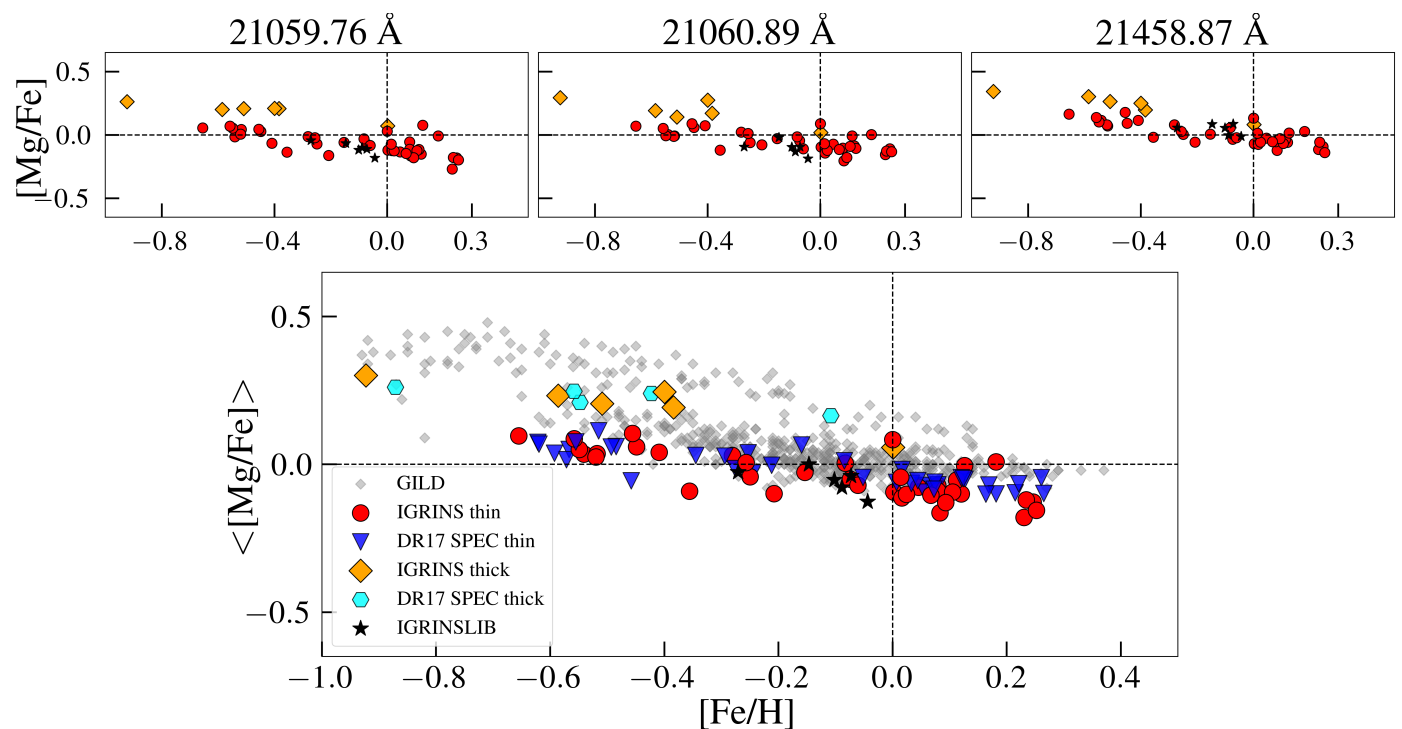


Fig. 9: The $[\text{Mg}/\text{Fe}]$ versus $[\text{Fe}/\text{H}]$ trends estimated from each Magnesium line (top row panels) and the trend from the mean of line-by-line $[\text{Mg}/\text{Fe}]$ estimates (bottom panel). The red circles (thin disc), orange diamonds (thick disc) and black star symbols (thin disc) in all panels represent the 44 solar neighborhood M giants and the six nearby M giants respectively. Gray diamonds in the bottom panel represent the stars in the Giants in the Local Disc (GILD) sample with parameters and abundances estimated from optical FIES spectra and shifted down by 0.1 dex. Blue inverted triangles (thin disc) and cyan hexagons (thick disc) represent the APOGEE spectroscopic estimates for the 43 solar neighborhood stars.

from each line is fitted with a Gaussian function. The dispersion estimated from this fit gives the uncertainty in abundances. Table A.10 lists the uncertainties from the individual elemental lines as well as the mean uncertainty corresponding to each elemental abundance for these seven stars. The mean abundance uncertainties range from 0.04-0.08 dex for $[\text{Mg}/\text{Fe}]$, 0.07-0.11 dex for $[\text{Si}/\text{Fe}]$, 0.04-0.07 dex for $[\text{Ca}/\text{Fe}]$ and 0.06-0.11 dex for $[\text{Ti}/\text{Fe}]$.

6.1. Magnesium (Mg)

We determined the magnesium abundances from three lines in the K band: 21059.76 Å, 21060.89 Å, 21458.87 Å. The two H band Mg I lines at 15740.70 Å and 15748.89 Å could not be used in this work since we find these two lines to be saturated based on their insensitivity to ± 0.2 dex variation in Mg abundances. In addition, the Mg abundances from these two lines are

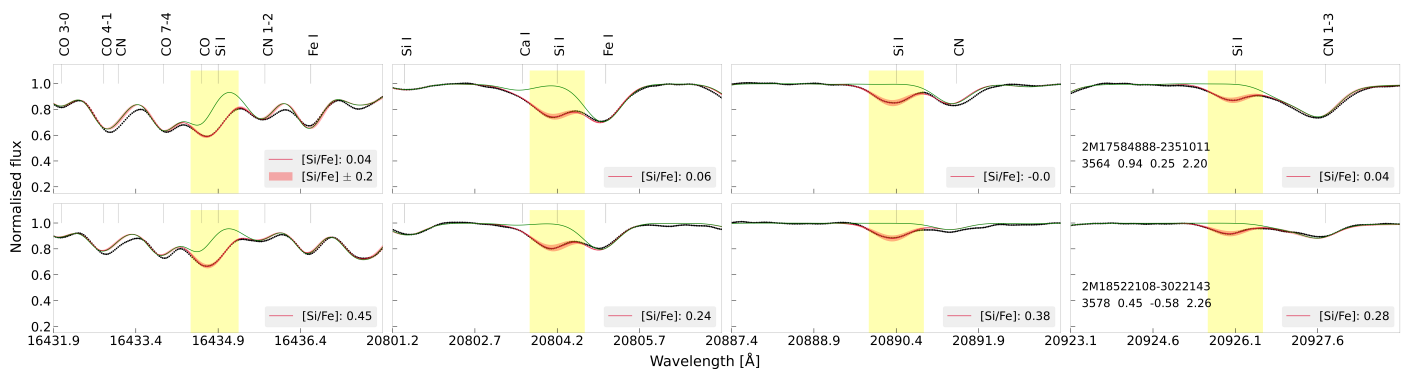
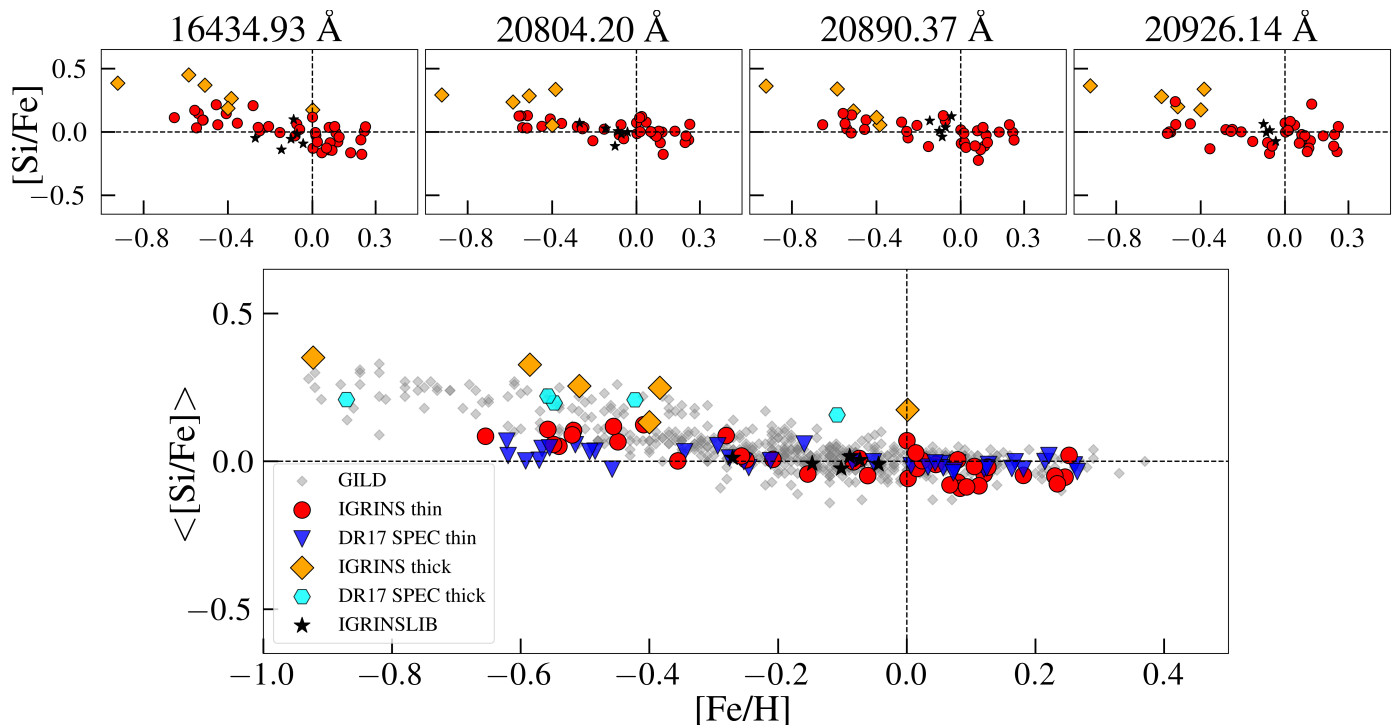


Fig. 10: Similar to Figure 8 but for silicon lines.


 Fig. 11: Similar to Figure 9 but for $[\text{Si}/\text{Fe}]$.

found to have strong correlation with the microturbulence (0.1–0.2 dex variation for $\Delta\xi_{\text{micro}} = \pm 0.2$ dex).

In the Figure 8, we plot the selected Mg lines in the observed spectra of one thin disc star (#40, top row panels) and one thick disc star (#44, bottom row panels) in black circles, the synthetic spectrum fit to these lines in red, and the variation in the fit resulting ± 0.2 dex change in the abundance value as red band. The yellow bands in each panel represent the line masks defined for the Mg lines (avoiding the neighboring lines) wherein the SME fits observed spectra by varying Magnesium abundance and finds the best synthetic spectra fit by chi-square minimisation. The green line shows the synthetic spectrum without Mg, also indicating any possible blends in the line. The stellar parameters estimated for each star is listed in the left most panels along with the derived abundance from each line in the corresponding panel.

We plot the Mg abundance trend ($[\text{Mg}/\text{Fe}]$ versus $[\text{Fe}/\text{H}]$) from each of these lines in the top five panels and the mean Mg abundance trend in the bottom panel of the Figure 9. In these plots, the red circles (thin disc) and orange diamonds (thick disc) represent the solar neighborhood sample and black star sym-

bols represent the six nearby M giants. In the bottom panel, the GILD Mg abundance trend is plotted as gray diamonds while the APOGEE spectroscopic Mg values for the 43 solar neighborhood stars (except #39) are plotted as blue inverted triangles (thin disc) and cyan hexagons (thick disc).

This is also evident in the negligible variation in the synthetic spectrum fit to the two H band lines for the ± 0.2 dex $[\text{Mg}/\text{Fe}]$ variation in Figure 8. The $[\text{Mg}/\text{Fe}]$ trend from all three K band lines show a decreasing trend with increasing metallicity, especially at supersolar metallicities (as expected from the chemical evolution models, see Matteucci 2021) and a clear enhancement in $[\text{Mg}/\text{Fe}]$ for thick disc stars compared to thin disc stars. $[\text{Mg}/\text{Fe}]$ values from the multiplet lines 21059.76 Å and 21060.89 Å are found to have sub solar $[\text{Mg}/\text{Fe}]$ at solar metallicity unlike those from the 21458.87 Å that pass through the solar value as expected. This line also has a comparatively accurate g -value as listed in NIST database with an accuracy grade of B+ (which means $\leq 7\%$). The line parameters we used for the two multiplet K band lines have been found to result in good synthetic spectrum fit to the lines in the high resolution Sun

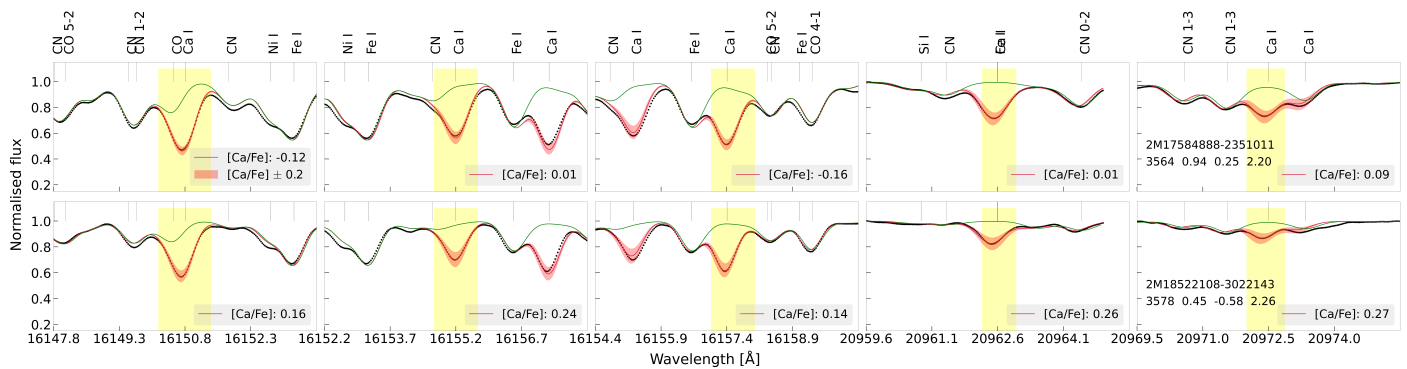
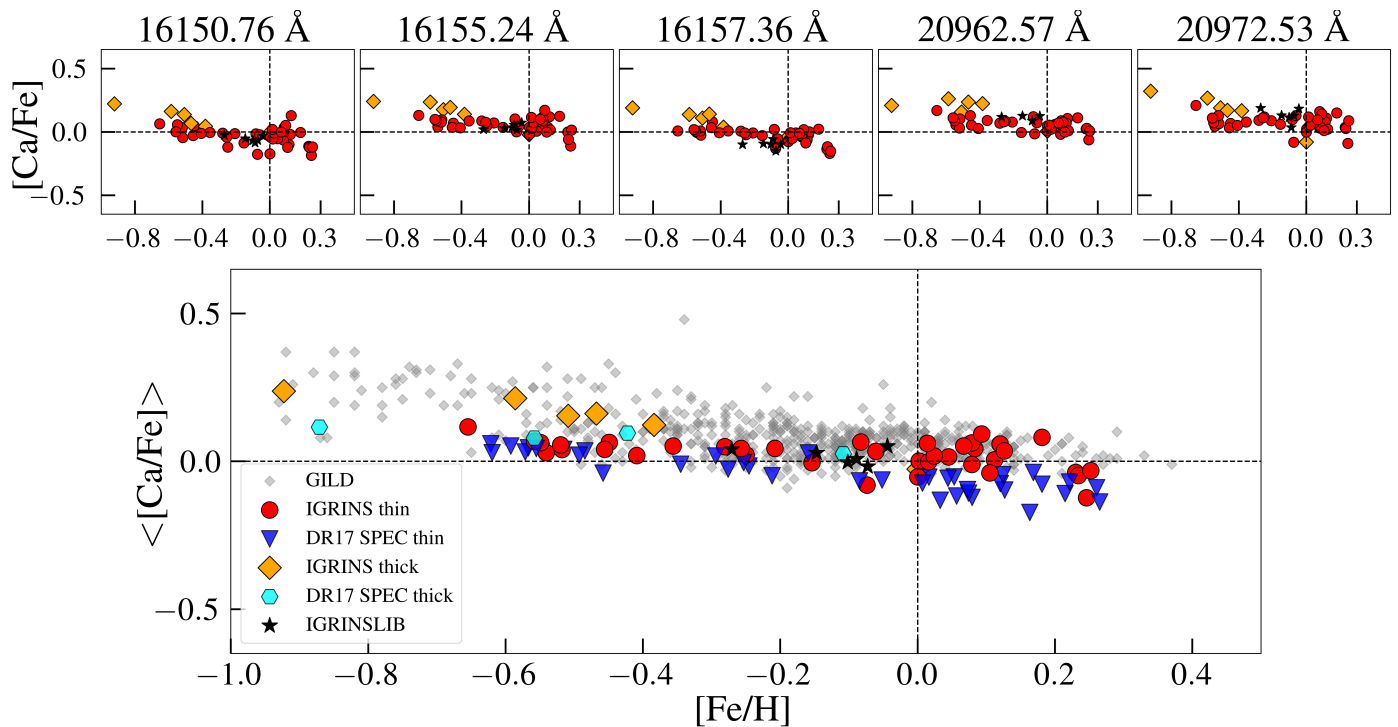


Fig. 12: Similar to Figure 8 but for calcium lines.


Fig. 13: Similar to Figure 9 but for $[Ca/Fe]$. The GILD $[Ca/Fe]$ have been shifted down by 0.05 dex to normalize the comparison sample to the solar value.

and Arcturus spectra. Nieuwmunster et al. (2023) using the same lines and line data, found similar low trend for inner bulge stars and warmer solar neighborhood K giants. We would also like to point out that the $[Mg/Fe]$ values determined from each line for the six nearby M giants are consistent with the corresponding trend obtained for the solar neighborhood stars.

We determined the mean $[Mg/Fe]$ for each star from the lines which are deemed to have good synthetic spectrum fit by visual check and not affected by noise or telluric lines. The individual and mean $[Mg/Fe]$ for each star along with the standard deviation value is listed in the Table A.6. Our mean $[Mg/Fe]$ trend shows a clear thin disc-thick disc dichotomy with enhanced values for thick disc stars. On comparison with the APOGEE DR17 spectroscopic $[Mg/Fe]$ values for the same stars, our mean abundances for thick and thin disc stars are consistent with APOGEE values. At the same time, both our and the APOGEE $[Mg/Fe]$ trends pass through subsolar $[Mg/Fe]$ at solar metallicity. Meanwhile, the $[Mg/Fe]$ trend for warmer stars in the GILD sample pass through supersolar $[Mg/Fe]$ values at solar metallicities

with a systematic difference of $\sim 0.1 - 0.2$ dex with respect to our $[Mg/Fe]$ trend. In Figure 9, we, therefore, shifted the GILD trend down by 0.1 dex in order to normalize this comparison sample to the solar value, to allow for a better comparison. We find that the LTE $[Mg/Fe]$ values for our stars agree well with the original GILD trend (see Section 6.5). The systematic difference between our trend and GILD trend might be caused by the use of NLTE grids in this work and LTE values in GILD.

6.2. Silicon (Si)

We determined $[Si/Fe]$ for the stars in the nearby M giant sample and the solar neighborhood sample from one line at 16434.93 \AA in the H band and three lines in the K band: 20804.20 \AA , 20890.37 \AA , and 20926.14 \AA . In Figure 10, we plot the selected Si lines in the observed spectra of one thin disc star (top row panels) and one thick disc star (bottom row panels) in black circles, the line masks in yellow band, the synthetic spectrum fit to these lines in red, the synthetic spectrum without the Si I feature

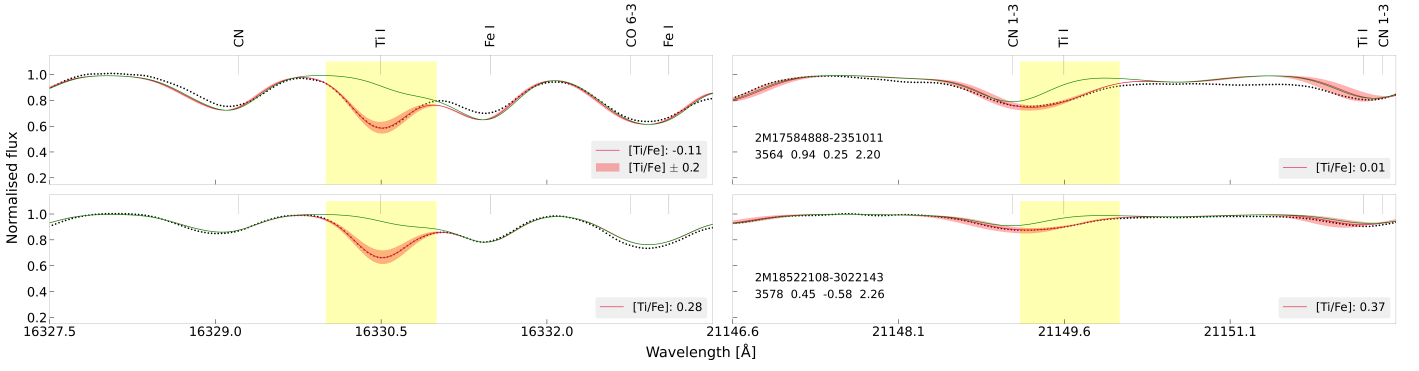
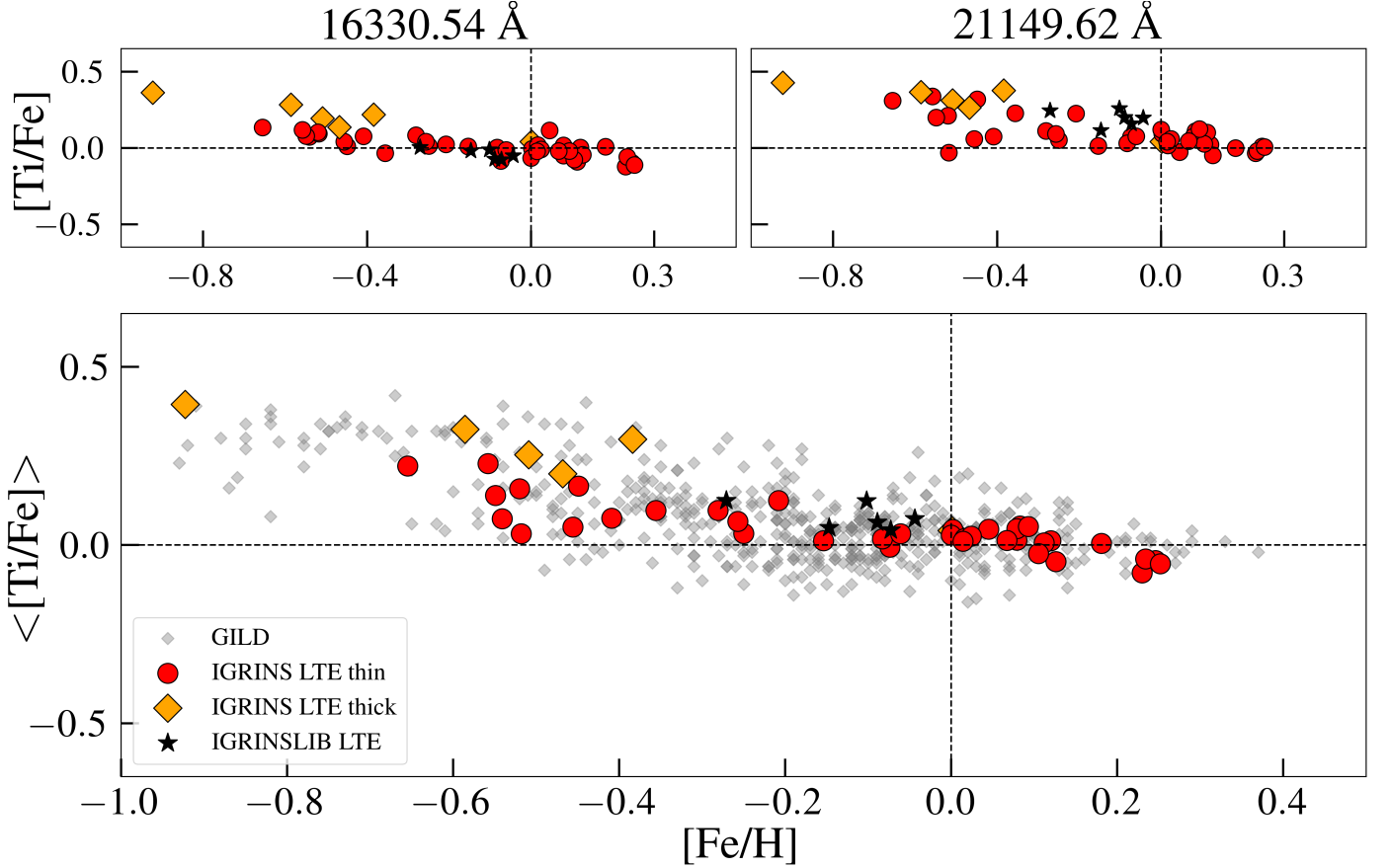


Fig. 14: Similar to Figure 8 but for titanium lines.


 Fig. 15: Similar to Figure 9 but for $[\text{Ti}/\text{Fe}]$.

in green, and the variation in the fit resulting ± 0.2 dex change in the abundance value as red band. The stellar parameters estimated for each star are listed in the left most panels along with the derived abundance from each line in the corresponding panel. In Figure 11 we plot our individual $[\text{Si}/\text{Fe}]$ trends in the top panels and the mean $[\text{Si}/\text{Fe}]$ in the bottom panel (red circles and black star symbols for thin disc stars and orange diamonds for thick disc stars) along with $[\text{Si}/\text{Fe}]$ from GILD sample (gray diamonds) and APOGEE DR17 (blue inverted triangles and cyan hexagons).

The synthetic spectrum fit to all four lines for the sample thin and thick disc stars in Figure 10 are reasonably good. We find enhancements in the mean $[\text{Si}/\text{Fe}]$ for all six thick disc stars. We note that there is only one good Si line for the solar metallicity thick disc star, #4 ($[\text{Fe}/\text{H}]=0.0$), from which we determine

high $[\text{Si}/\text{Fe}]$ value of ~ 0.18 dex. This could be the reason for the distinctly high $[\text{Si}/\text{Fe}]$ but lower abundance values of other alpha elements for this star. The mean thin disc trend of the solar neighborhood and nearby M giant sample is consistent with the GILD sample thin disc trend at all metallicities, but we find $\sim 0.05 - 0.1$ dex enhancement in our thick disc trend compared to the GILD thick disc trend. Similar difference is seen with respect to the APOGEE $[\text{Si}/\text{Fe}]$ abundances of thick disc stars and also compared to the $[\text{Fe}/\text{H}] < -0.5$ thin disc stars. Overall, the thin-disc trend shows a small scatter and the thick-disk trend is clearly elevated in $[\text{Si}/\text{Fe}]$.

6.3. Calcium (Ca)

We used five calcium absorption lines to determine $[Ca/Fe]$, three in the H band: 16150.76 Å, 16155.24 Å, and 16157.36 Å and two in the K band: 20962.57 Å, and 20972.53 Å. In the Figure 12, we plot the selected Ca lines in the observed spectra of one thin disc star (top row panels) and one thick disc star (bottom row panels) in black circles, the line masks in yellow band, the synthetic spectrum fit to these lines in red, the synthetic spectrum without the Ca I feature in green, and the variation in the fit resulting ± 0.2 dex change in the abundance value as red band. The stellar parameters estimated for each star is listed in the left most panels along with the derived abundance from each line in the corresponding panel. Figure 13 shows the $[Ca/Fe]$ trends from the six individual lines in the top panels and the mean $[Ca/Fe]$ trend from the chosen set of good lines for each star from the solar neighborhood sample and six nearby M giants in the bottom panel.

As shown in the Figure 12, we could fit all five lines very well. In addition, these lines are strongly dependent on the Ca abundance as indicated by the significant variation in the synthetic spectrum with ± 0.2 dex variation in $[Ca/Fe]$. The $[Ca/Fe]$ trends from all six lines follow a downward trend, although with a shallower slope than for, e.g., $[Mg/Fe]$. Above solar metallicity $[Ca/Fe]$ seem to at least level off to decrease again at $[Fe/H] > 0.2$ dex. A larger sample would clarify this observation. The mean $[Ca/Fe]$ values follow the same trend and the five metal poor thick disc stars have enhanced mean abundances compared to the thin disc stars. We do not find similar enhancement for the solar metallicity thick disc star. Unlike the case of Mg and Si, there is no clear separation between the thin and thick disc stars in the $[Ca/Fe]$ trend from the GILD sample. Compared to the GILD trend, our mean $[Ca/Fe]$ trend is systematically lower by 0.05 dex but pass through solar $[Ca/Fe]$ at solar metallicity. Similar to Mg, we have, therefore, shifted the GILD trend down by 0.05 dex in order to normalize this comparison sample to the solar value, to allow for a better comparison. The $[Ca/Fe]$ trend from APOGEE DR17 sample follows a downward trend that continues to decrease at higher metallicities. The DR17 $[Ca/Fe]$ values are lower for the thick disc stars and thus do not show any clear separation with respect to the thin disc stars.

6.4. Titanium (Ti)

Only two lines have been used to determine $[Ti/Fe]$, one in the H band: 16330.54 Å and one in the K band: 21149.62 Å. In Figure 14, we plot the selected Ti lines in the observed spectra of one thin disc star (top row panels) and one thick disc star (bottom row panels) in black circles, the line masks in yellow band, the synthetic spectrum fit to these lines in red, the synthetic spectrum without the Ti I feature in green, and the variation in the fit resulting ± 0.2 dex change in the abundance value as red band. The stellar parameters estimated for each star is listed in the left most panels along with the derived abundance from each line in the corresponding panel. Similar to Mg, Si and Ca, Figure 15 shows the $[Ti/Fe]$ trends from the two individual lines in the top two panels and the mean $[Ti/Fe]$ trend in the bottom panel.

Compared to the H band line at 16330.54 Å, the K band line at 21149.62 Å is weaker and blended with CN ($\nu=1-3$). The $[Ti/Fe]$ trend determined using the line at 16330.54 Å is found to have lower scatter at sub solar metallicities compared to the trend determined from the line at 21149.62 Å. This may be attributed to the CN ($\nu = 1-3$) blend in the left wing of the K band

line as can be seen in Figure 14. This scatter is carried forward to the mean $[Ti/Fe]$ trend for low metallicity stars ($[Fe/H] < -0.4$ dex). Yet the metal poor thick disc stars show clear enhancement compared to the thin disc stars. Furthermore, the mean $[Ti/Fe]$ abundance trend is consistent with the optical $[Ti/Fe]$ trend from the GILD sample. Unfortunately, APOGEE DR17 do not provide $[Ti/Fe]$ measurements for the 44 stars. It has been noted that the Ti I lines in the APOGEE wavelength regime (H band) are very sensitive to T_{eff} (Jönsson et al. 2018, 2020). Hence, it is reassuring for our method and especially for our determined T_{eff} that the $[Ti/Fe]$ determined using our stellar parameters are consistent with the trend from optical spectra.

6.5. LTE and non-LTE comparison

As mentioned in the Section 3, we have applied NLTE corrections to the abundance measurements of Mg, Si and Ca. In addition, we estimated abundances for all three elements without applying NLTE corrections. Figure 16 shows the NLTE (brown) and LTE trends (cyan) for all three elements as a function of $[Fe/H]$. The NLTE-LTE difference for $[Mg/Fe]$ and $[Ca/Fe]$ range from -0.05 to -0.15 dex and there is no significant NLTE-LTE difference for $[Si/Fe]$. Thus applying NLTE corrections lower the abundance values for Mg and Si.

7. Conclusions

For abundance studies, a general method to determine the important stellar parameters for M giants is needed. For example, in order to study stellar abundances and the chemical evolution of stellar populations in dust obscured regions, like the inner bulge and Galactic Center region, the intrinsically bright M giants observed in the near-infrared is an optimal option. Not only is the extinction lower in the infrared, but cool stars, such as M giants, can only be analysed in the near-IR due to the ubiquitous TiO features in optical spectra of stars with $T_{\text{eff}} < 4000$ K. Due to uncertainties in photometric methods, a method to determine the stellar parameters for M giants from the near-IR spectra themselves is needed. Such a method would thus open up the possibility to efficiently allow these regions to be analysed.

Thus, in this quest to determine reliable stellar parameters and elemental abundances of M giant stars from their near infrared spectra, we have developed an iterative method, tested for $3400 \lesssim T_{\text{eff}} \lesssim 4000$ K, presented here. We have used high resolution ($R \sim 45,000$) spectra in the H band observed with the IGRINS spectrometer. IGRINS spectra cover the entire wavelength range of the H and K bands ($\sim 14\,000$ Å to $25\,000$ Å) which provides a wealth of spectral lines for the subsequent study of stellar abundances too.

Since T_{eff} is one of the most crucial fundamental stellar parameter, we started off by identifying ~ 15 to 20 T_{eff} sensitive molecular OH lines in the H band based on our investigations using the APOGEE M giant spectra and their parameters provided in the DR17 catalog. In addition to T_{eff} , the OH line strengths also depend on the oxygen abundance resulting in a degeneracy between T_{eff} and oxygen abundance. Hence we fix the oxygen abundance based on the metallicity of the star following the $[O/Fe]$ versus $[Fe/H]$ trend in Amarsi et al. (2019) for thin and thick disc stars (Figure 1). It is reassuring that even for an initial misidentification of the stellar population, this will be able to be remedied by determining, e.g., the $[Mg/Fe]$ abundance. This will clearly show which population the star actually belongs to (see Section 5.2).

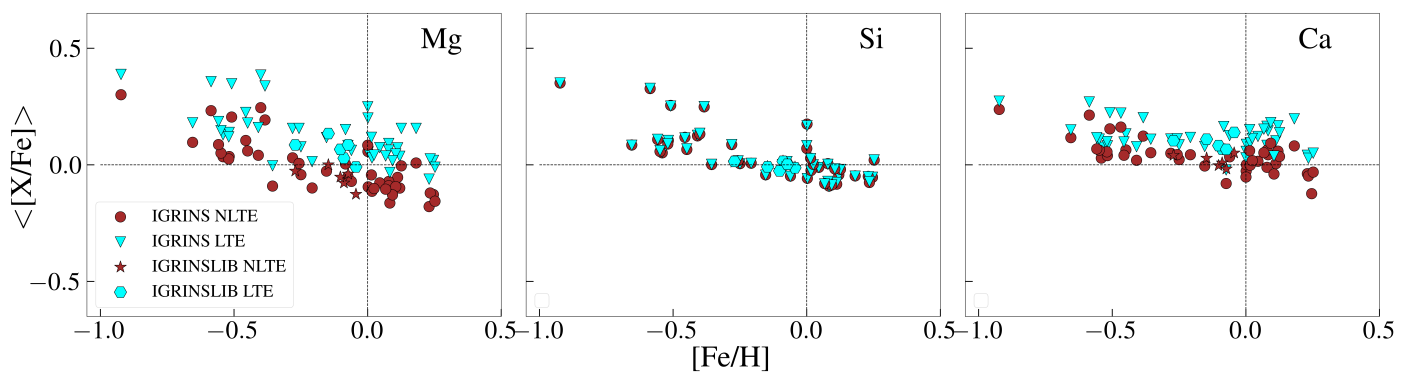


Fig. 16: NLTE (brown) and LTE (cyan) abundance trends as a function of $[Fe/H]$ for $[Mg/Fe]$, $[Si/Fe]$ and $[Ca/Fe]$ estimated for 44 solar neighborhood M giants (circle symbol - NLTE and inverted triangle symbol - LTE) and six nearby M giants (star symbol - NLTE and hexagon symbol - LTE). There is negligible difference between NLTE and LTE measurements for Si while Mg and Ca show 0.05 - 0.15 dex differences.

After the initial assumption of the stellar population, we start with initial T_{eff} and $[Fe/H]$ of 3500 K and 0.0 dex, respectively. The $\log g$ value is chosen to be 0.65 dex from the 10 Gyr Yonsei-Yale (YY) isochrones corresponding to the initial assumed T_{eff} and $[Fe/H]$ by means of simple linear interpolation (Rich et al. 2017). Our method requires multiple iterations wherein firstly we determine T_{eff} , $[Fe/H]$, ξ_{micro} , $[C/Fe]$ and $[N/Fe]$ using SME by fitting the selected set of OH, CN, CO and Fe lines. We then determine $\log g$ based on the newly determined T_{eff} and $[Fe/H]$ from the 10 Gyr YY isochrones. Similarly, the oxygen abundance is updated corresponding to the new $[Fe/H]$. With the updated $\log g$, and oxygen abundance, we determine new values of T_{eff} , $[Fe/H]$, ξ_{micro} , $[C/Fe]$ and $[N/Fe]$ and this cycle is repeated until there is negligible differences between the latest and previously determined values of all free parameters (Figure 2). A final check of the assumed stellar population is then done based on the determined α abundances, most importantly the $[Mg/Fe]$ abundance.

We validate our method by deriving the stellar parameters for six nearby well-studied M-giants with spectra from the IGRINS spectral library. Further, we demonstrate the accuracy and precision by determining the α -element trends versus metallicity for 44 solar neighbourhood M giants from our two IGRINS runs on Gemini (We also include the six M giants in the α -element trends versus metallicity). 43 of the stars from our two IGRINS runs have also been analysed in APOGEE. The effective temperatures that we derive from our new method agree excellently with the six nearby, well-studied M giants (in Fig. 3) which indicates that the accuracy is indeed high. For the 43 solar neighborhood M giants, we find excellent agreement with APOGEE for T_{eff} , $\log g$, $[Fe/H]$, ξ_{micro} , $[C/Fe]$, $[N/Fe]$, and $[O/Fe]$ with mean differences and scatter (our method - APOGEE) of -67 ± 33 K, -0.31 ± 0.15 dex, 0.02 ± 0.05 dex, 0.22 ± 0.13 km/s, -0.05 ± 0.06 dex, 0.06 ± 0.06 dex, and 0.02 ± 0.09 dex, respectively. Furthermore, the tight offset with a small dispersion compared to APOGEE's T_{eff} points to a high precision in both our derived temperatures and those derived from the APOGEE pipeline (Figure 5). The large scatter in the T_{eff} determined using photometric methods like the IRFM and $T_{\text{eff}}-(V-K)$ relations further emphasizes the necessity of developing such spectroscopic methods to determine stellar parameters.

Typical uncertainties in the stellar parameters corresponding to ± 0.15 dex uncertainty in $[O/Fe]$ are found to be ± 100 K in T_{eff} , ± 0.2 dex in $\log g$, ± 0.1 dex in $[Fe/H]$, ± 0.1 km/s in ξ_{micro} , ± 0.1 dex in $[C/Fe]$, and ± 0.1 dex in $[N/Fe]$. Another source of

uncertainty is the use of 10 Gyr YY isochrone to constrain $\log g$. However, we find that the difference in derived surface gravity is less than 0.1 dex on using a 2 Gyr YY isochrone instead of the 10 Gyr one.

The α -element trends versus metallicity for Mg, Si, Ca and Ti shows excellent agreement with both APOGEE DR17 trends for the same stars as well as with the GILD optical trends. We also find clear enhancement in abundances for thick disc stars.

The two main limitations of our method are fixing the oxygen abundance and the use of theoretical isochrones to constrain $\log g$. We explored in detail the effect of fixing wrong oxygen abundances on the derived stellar parameters, and found ways to remedy such wrong assumptions. To test the accuracy of the $\log g$ values we estimated from isochrones in our method, it is imperative to test our method on well-studied benchmark M giant stars (Heiter et al. 2015). We also need to increase the sample size of the solar neighborhood M giants to cover full stellar parameter range, especially at temperatures lower than 3500 K.

As mentioned in the Section 1, T_{eff} - line depth ratios (LDRs) relations have been proposed by many recent studies (Fukue et al. 2015, Taniguchi et al. 2018, Taniguchi et al. 2021, Matsunaga et al. 2021, Afşar et al. 2023) especially in the near infrared wavelength regimes (0.97 - 2.4 μm) for late type giants with broad range of T_{eff} s (3500 to 5400 K). Our method has only been tested on the cool stars ($T_{\text{eff}} < 4000$ K) and we need to apply our method on warmer stars with weaker molecular absorption lines in order to test its limits. At the same time, the outcome from the LDR methods are limited to T_{eff} alone, while we determine the fundamental stellar parameters as well as C, N abundances with our method.

To summarize, we have developed a method to determine reliable stellar parameters for M giants from their near infrared spectra, which can be made fully automatic for future near-IR surveys.

Acknowledgements. We thank the anonymous referee for the constructive comments and suggestions that improved the quality and aesthetics of the paper. G.N. acknowledges the support from the Wenner-Gren Foundations and the Royal Physiographic Society in Lund through the Stiftelsen Walter Gyllenbergs fond. G.N. thanks Henrik Jönsson for enlightening discussions. N.R. acknowledge support from the Royal Physiographic Society in Lund through the Stiftelsen Walter Gyllenbergs fond and Märta och Erik Holmbergs donation and from Magnus Bergvalls stiftelse. This work used The Immersion Grating Infrared Spectrometer (IGRINS) was developed under a collaboration between the University of Texas at Austin and the Korea Astronomy and Space Science Institute (KASI) with the financial support of the US National Science Foundation under grants AST-1229522, AST-1702267 and AST-1908892, McDonald Observatory of the University of Texas at Austin, the Korean GMT Project of KASI, the Mt. Cuba

Astronomical Foundation and Gemini Observatory. These results made use of the Lowell Discovery Telescope (LDT) at Lowell Observatory. Lowell is a private, non-profit institution dedicated to astrophysical research and public appreciation of astronomy and operates the LDT in partnership with Boston University, the University of Maryland, the University of Toledo, Northern Arizona University and Yale University. This paper includes data taken at The McDonald Observatory of The University of Texas at Austin.

The following software and programming languages made this research possible: TOPCAT (version 4.6; Taylor 2005); Python (version 3.8) and its packages ASTROPY (version 5.0; Astropy Collaboration et al. 2022), SCIPY (Virtanen et al. 2020), MATPLOTLIB (Hunter 2007) and NUMPY (van der Walt et al. 2011).

References

- Afşar, M., Bozkurt, Z., Böcek Topcu, G., et al. 2023, arXiv e-prints, arXiv:2303.15030
- Amarsi, A. M., Lind, K., Asplund, M., Barklem, P. S., & Collet, R. 2016, *MNRAS*, 463, 1518
- Amarsi, A. M., Lind, K., Osorio, Y., et al. 2020, *A&A*, 642, A62
- Amarsi, A. M., Nissen, P. E., & Skúladóttir, Á. 2019, *A&A*, 630, A104
- Amarsi, A. M., Nordlander, T., Barklem, P. S., et al. 2018, *A&A*, 615, A139
- Anstee, S. D. & O'Mara, B. J. 1991, *MNRAS*, 253, 549
- Anstee, S. D. & O'Mara, B. J. 1995, *MNRAS*, 276, 859
- Astropy Collaboration, Price-Whelan, A. M., Lim, P. L., et al. 2022, *ApJ*, 935, 167
- Baines, E. K., Thomas Armstrong, J., Clark, J. H., et al. 2021, *AJ*, 162, 198
- Barklem, P. S. & O'Mara, B. J. 1997, *MNRAS*, 290, 102
- Barklem, P. S., O'Mara, B. J., & Ross, J. E. 1998, *MNRAS*, 296, 1057
- Bessell, M. S. & Brett, J. M. 1988, *PASP*, 100, 1134
- Bessell, M. S., Castelli, F., & Plez, B. 1998, *A&A*, 333, 231
- Biemont, E., Roland, G., Delbouille, L., & Brault, J. W. 1985, *A&AS*, 61, 107
- Brault, J. & Noyes, R. 1983, *ApJ*, 269, L61
- Brooke, J. S. A., Bernath, P. F., Western, C. M., et al. 2016, *J. Quant. Spectr. Rad. Transf.*, 168, 142
- Buder, S., Sharma, S., Kos, J., et al. 2021, *MNRAS*, 506, 150
- Casagrande, L. 2008, *Physica Scripta Volume T*, 133, 014020
- Casagrande, L., Lin, J., Rains, A. D., et al. 2021, *MNRAS*, 507, 2684
- Casagrande, L., Ramírez, I., Meléndez, J., Bessell, M., & Asplund, M. 2010, *A&A*, 512, A54
- Casagrande, L. & Vandenberg, D. A. 2014, *MNRAS*, 444, 392
- Casagrande, L., Wolf, C., Mackey, A. D., et al. 2019, *MNRAS*, 482, 2770
- Civiš, S., Ferus, M., Chernov, V. E., & Zanozina, E. M. 2013, *A&A*, 554, A24
- Cox, N. L. J., Cami, J., Kaper, L., et al. 2014, *A&A*, 569, A117
- de Zeeuw, T., Tamai, R., & Liske, J. 2014, *The Messenger*, 158, 3
- Demarque, P., Woo, J.-H., Kim, Y.-C., & Yi, S. K. 2004, *ApJS*, 155, 667
- Ebenbichler, A., Postel, A., Przybilla, N., et al. 2022, *A&A*, 662, A81
- Elyajouri, M., Lallement, R., Monreal-Ibero, A., Capitanio, L., & Cox, N. L. J. 2017, *A&A*, 600, A129
- Fukue, K., Matsunaga, N., Yamamoto, R., et al. 2015, *ApJ*, 812, 64
- Gaia Collaboration, Brown, A. G. A., Vallenari, A., et al. 2021, *A&A*, 649, A1
- Galazutdinov, G. A., Lee, J.-J., Han, I., et al. 2017, *MNRAS*, 467, 3099
- García Pérez, A. E., Allende Prieto, C., Holtzman, J. A., et al. 2016, *AJ*, 151, 144
- Geballe, T. R. 2016, in *Journal of Physics Conference Series*, Vol. 728, *Journal of Physics Conference Series*, 062005
- Geballe, T. R., Najarro, F., Figer, D. F., Schlegelmilch, B. W., & de La Fuente, D. 2011, *Nature*, 479, 200
- Genoni, M., Riva, M., Pariani, G., Aliverti, M., & Moschetti, M. 2016, in *Society of Photo-Optical Instrumentation Engineers (SPIE) Conference Series*, Vol. 9911, *Modeling, Systems Engineering, and Project Management for Astronomy VI*, ed. G. Z. Angeli & P. Dierickx, 99112L
- Ghosh, S., Mondal, S., Das, R., & Khata, D. 2019, *MNRAS*, 484, 4619
- Ghosh, S., Ninan, J. P., & Ojha, D. K. 2022, *MNRAS*, 511, 814
- Ghosh, S., Ojha, D. K., & Ninan, J. P. 2021, *MNRAS*, 501, 4596
- Gray, D. F. 2008, *The Observation and Analysis of Stellar Photospheres*
- Grevesse, N., Asplund, M., & Sauval, A. J. 2007, *Space Sci. Rev.*, 130, 105
- Guercó, R., Cunha, K., Smith, V. V., et al. 2019, *ApJ*, 885, 139
- Gully-Santiago, M., Wang, W., Deen, C., & Jaffe, D. 2012, in *Society of Photo-Optical Instrumentation Engineers (SPIE) Conference Series*, Vol. 8450, *Modern Technologies in Space- and Ground-based Telescopes and Instrumentation II*, ed. R. Navarro, C. R. Cunningham, & E. Prieto, 84502S
- Gustafsson, B., Edvardsson, B., Eriksson, K., et al. 2008, *A&A*, 486, 951
- Hamano, S., Kobayashi, N., Kawakita, H., et al. 2022, *ApJS*, 262, 2
- Han, J.-Y., Yuk, I.-S., Ko, K., et al. 2012, in *Society of Photo-Optical Instrumentation Engineers (SPIE) Conference Series*, Vol. 8550, *Optical Systems Design 2012*, ed. D. G. Smith, J.-L. M. Tissot, L. Mazuray, T. E. Kidger, F. Wyrowski, J. M. Raynor, R. Wartmann, S. David, A. Erdmann, A. P. Wood, P. Benítez, & M. C. de la Fuente, 85501B
- He, B., Fan, D., Cui, C., et al. 2017, in *Astronomical Society of the Pacific Conference Series*, Vol. 512, *Astronomical Data Analysis Software and Systems XXV*, ed. N. P. F. Lorente, K. Shortridge, & R. Wayth, 153
- Heiter, U., Jofré, P., Gustafsson, B., et al. 2015, *A&A*, 582, A49
- Hinkle, K., Wallace, L., & Livingston, W. 1995, *PASP*, 107, 1042
- Holtzman, J. A., Hasselquist, S., Shetrone, M., et al. 2018, *AJ*, 156, 125
- Hunter, J. D. 2007, *Computing in Science and Engineering*, 9, 90
- Jeong, U., Chun, M.-Y., Oh, J. S., et al. 2014, in *Society of Photo-Optical Instrumentation Engineers (SPIE) Conference Series*, Vol. 9154, *High Energy, Optical, and Infrared Detectors for Astronomy VI*, ed. A. D. Holland & J. Beletic, 91541X
- Jian, M., Matsunaga, N., & Fukue, K. 2019, *MNRAS*, 485, 1310
- Jofré, P., Heiter, U., & Soubiran, C. 2019, *ARA&A*, 57, 571
- Jönsson, H., Allende Prieto, C., Holtzman, J. A., et al. 2018, *AJ*, 156, 126
- Jönsson, H., Holtzman, J. A., Allende Prieto, C., et al. 2020, *AJ*, 160, 120
- Jönsson, H., Ryde, N., Harper, G. M., Richter, M. J., & Hinkle, K. H. 2014, *ApJ*, 789, L41
- Jönsson, H., Ryde, N., Nordlander, T., et al. 2017, *A&A*, 598, A100
- Kupka, F. G., Ryabchikova, T. A., Piskunov, N. E., Stempels, H. C., & Weiss, W. W. 2000, *Baltic Astronomy*, 9, 590
- Kurucz, R. L. 2007, Robert L. Kurucz on-line database of observed and predicted atomic transitions
- Kurucz, R. L. 2014, Robert L. Kurucz on-line database of observed and predicted atomic transitions
- Kurucz, R. L. 2016, Robert L. Kurucz on-line database of observed and predicted atomic transitions
- Lawler, J. E., Guzman, A., Wood, M. P., Sneden, C., & Cowan, J. J. 2013, *ApJS*, 205, 11
- Lebzelter, T., Hinkle, K. H., Straniero, O., et al. 2019, *ApJ*, 886, 117
- Lee, J.-J., Gullikson, K., & Kaplan, K. 2017, *Igrins/Plp 2.2.0*, Zenodo
- Li, G., Gordon, I. E., Rothman, L. S., et al. 2015, *ApJS*, 216, 15
- Lind, K., Amarsi, A. M., Asplund, M., et al. 2017, *MNRAS*, 468, 4311
- Mace, G., Sokal, K., Lee, J.-J., et al. 2018, in *Society of Photo-Optical Instrumentation Engineers (SPIE) Conference Series*, Vol. 10702, *Ground-based and Airborne Instrumentation for Astronomy VII*, ed. C. J. Evans, L. Simard, & H. Takami, 107020Q
- Maiolino, R., Haehnelt, M., Murphy, M. T., et al. 2013, arXiv e-prints, arXiv:1310.3163
- Matsunaga, N., Jian, M., Taniguchi, D., & Elgueta, S. S. 2021, *MNRAS*, 506, 1031
- Matteucci, F. 2021, *A&A Rev.*, 29, 5
- Mawet, D., Fitzgerald, M., Konopacky, Q., et al. 2019, in *Bulletin of the American Astronomical Society*, Vol. 51, 134
- Minchev, I., Steinmetz, M., Chiappini, C., et al. 2017, *ApJ*, 834, 27
- Montelius, M., Forsberg, R., Ryde, N., et al. 2022, arXiv e-prints, arXiv:2202.00691
- Moon, B., Wang, W., Park, C., et al. 2012, in *Society of Photo-Optical Instrumentation Engineers (SPIE) Conference Series*, Vol. 8450, *Modern Technologies in Space- and Ground-based Telescopes and Instrumentation II*, ed. R. Navarro, C. R. Cunningham, & E. Prieto, 845048
- Mozurkewich, D., Armstrong, J. T., Hindsley, R. B., et al. 2003, *AJ*, 126, 2502
- Nandakumar, G., Ryde, N., Montelius, M., et al. 2022, *A&A*, 668, A88
- Nieuwmanster, N., Nandakumar, G., Spitoni, E., et al. 2023, arXiv e-prints, arXiv:2301.10271
- Nissen, P. E., Hoeg, E., & Schuster, W. J. 1997, in *ESA Special Publication*, Vol. 402, *Hipparcos - Venice '97*, ed. R. M. Bonnet, E. Høg, P. L. Bernacca, L. Emiliani, A. Blaauw, C. Turon, J. Kovalevsky, L. Lindegren, H. Hassan, M. Bouffard, B. Strim, D. Heger, M. A. C. Perryman, & L. Woltjer, 225-230
- Oh, J. S., Park, C., Cha, S.-M., et al. 2014, in *Society of Photo-Optical Instrumentation Engineers (SPIE) Conference Series*, Vol. 9147, *Ground-based and Airborne Instrumentation for Astronomy V*, ed. S. K. Ramsay, I. S. McLean, & H. Takami, 914739
- Park, C., Jaffe, D. T., Yuk, I.-S., et al. 2014, in *Society of Photo-Optical Instrumentation Engineers (SPIE) Conference Series*, Vol. 9147, *Ground-based and Airborne Instrumentation for Astronomy V*, ed. S. K. Ramsay, I. S. McLean, & H. Takami, 91471D
- Park, S., Lee, J.-E., Kang, W., et al. 2018, *ApJS*, 238, 29
- Pinsonneault, M. H., Elsworth, Y. P., Tayar, J., et al. 2018, *ApJS*, 239, 32
- Piskunov, N. E., Kupka, F., Ryabchikova, T. A., Weiss, W. W., & Jeffery, C. S. 1995, *A&AS*, 112, 525
- Ramírez, I. & Allende Prieto, C. 2011, *ApJ*, 743, 135
- Randich, S., Gilmore, G., Magrini, L., et al. 2022, *A&A*, 666, A121
- Rich, R. M., Ryde, N., Thorsbro, B., et al. 2017, *AJ*, 154, 239
- Richichi, A., Fabbri, L., Ragland, S., & Scholz, M. 1999, *A&A*, 344, 511

- Ryabchikova, T., Piskunov, N., Kurucz, R. L., et al. 2015, *Phys. Scr*, 90, 054005
- Ryde, N. & Schultheis, M. 2015, *A&A*, 573, A14
- Santos-Peral, P., Recio-Blanco, A., de Laverny, P., Fernández-Alvar, E., & Ordenovic, C. 2020, *A&A*, 639, A140
- Sawczynec, E., Mace, G., Gully-Santiago, M., & Jaffe, D. 2022, in *American Astronomical Society Meeting Abstracts*, Vol. 54, *American Astronomical Society Meeting Abstracts*, 203.06
- Schlegel, D. J., Finkbeiner, D. P., & Davis, M. 1998, *ApJ*, 500, 525
- Schultheis, M., Ryde, N., & Nandakumar, G. 2016, *A&A*, 590, A6
- Sharma, K., Prugniel, P., & Singh, H. P. 2016, *A&A*, 585, A64
- Skidmore, W. e. a. 2022, Detailed Science Case 2022, Tech. rep., tMT.PSC.TEC.07.007.CCR03
- Smith, V. V., Cunha, K., Shetrone, M. D., et al. 2013, *ApJ*, 765, 16
- Smith, V. V. & Lambert, D. L. 1990, *ApJS*, 72, 387
- Snedden, C., Lucatello, S., Ram, R. S., Brooke, J. S. A., & Bernath, P. 2014, *ApJS*, 214, 26
- Steinmetz, M., Matijevič, G., Enke, H., et al. 2020, *AJ*, 160, 82
- Taniguchi, D., Matsunaga, N., Jian, M., et al. 2021, *MNRAS*, 502, 4210
- Taniguchi, D., Matsunaga, N., Kobayashi, N., et al. 2018, *MNRAS*, 473, 4993
- Taylor, M. B. 2005, in *Astronomical Society of the Pacific Conference Series*, Vol. 347, *Astronomical Data Analysis Software and Systems XIV*, ed. P. Shopbell, M. Britton, & R. Ebert, 29
- Thorsbro, B., Ryde, N., Rich, R. M., et al. 2020, *ApJ*, 894, 26
- Thorsbro, B., Ryde, N., Schultheis, M., et al. 2018, *ApJ*, 866, 52
- Tody, D. 1993, in *ASP Conf. Ser. 52: Astronomical Data Analysis Software and Systems II*, ed. R. J. Hanisch, R. J. V. Brissenden, & J. Barnes, 173
- Tsuji, T. 1981, *A&A*, 99, 48
- Valenti, J. A. & Piskunov, N. 1996, *A&AS*, 118, 595
- Valenti, J. A. & Piskunov, N. 2012, *SME: Spectroscopy Made Easy*, astrophysics Source Code Library
- van der Walt, S., Colbert, S. C., & Varoquaux, G. 2011, *Computing in Science and Engineering*, 13, 22
- Virtanen, P., Gommers, R., Oliphant, T. E., et al. 2020, *Nature Methods*, 17, 261
- Wallace, L. & Livingston, W. 2003, *An atlas of the solar spectrum in the infrared from 1850 to 9000 cm⁻¹ (1.1 to 5.4 micrometer)*
- Wang, W., Gully-Santiago, M., Deen, C., Mar, D. J., & Jaffe, D. T. 2010, in *Society of Photo-Optical Instrumentation Engineers (SPIE) Conference Series*, Vol. 7739, *Modern Technologies in Space- and Ground-based Telescopes and Instrumentation*, ed. E. Atad-Ettinger & D. Lemke, 77394L
- Yuk, I.-S., Jaffe, D. T., Barnes, S., et al. 2010, in *Society of Photo-Optical Instrumentation Engineers (SPIE) Conference Series*, Vol. 7735, *Ground-based and Airborne Instrumentation for Astronomy III*, ed. I. S. McLean, S. K. Ramsay, & H. Takami, 77351M

Appendix A: Tables

Table A.1: Line parameters of Fe I lines used in this work.

Element	Wavelength (Å)	log (gf)	Broadening by H ^a	α
Fe	15485.454 ³	-0.828 ^{3*}	-7.290	
	15490.881 ³	0.789 ³	1618 ¹	0.325
	15500.799 ³	0.789 ^{3*}	1772 ¹	0.320
	15501.320 ³	0.789 ^{3*}	1620 ¹	0.325
	15502.174 ³	-1.034 ^{3*}	1876 ¹	0.317
	15662.013 ³	0.145 ^{3*}	1326 ²	0.235
	15878.444 ³	-0.339 ^{3*}	-7.450	
	16153.247 ³	-0.682 ^{3*}	924 ²	0.229
	16165.029 ³	0.782 ^{3*}	1598 ²	0.325
	16171.930 ³	-0.399 ^{3*}	1858 ²	0.373
	16174.975 ³	0.201 ^{3*}	1861 ¹	0.316
	16177.085 ³	-1.089 ^{3*}	-7.330	
	16179.583 ³	0.118 ^{3*}	1600 ¹	0.325
	16180.900 ³	0.203 ^{3*}	1431 ¹	0.329
	16182.170 ³	-0.805 ^{3*}	1599 ¹	0.325
	16185.799 ³	0.211 ^{3*}	1919 ¹	0.313
	16245.763 ³	-0.652 ^{3*}	1602 ¹	0.325
	16246.458 ⁴	-0.106 ^{3*}	1419 ¹	0.329
	16258.912 ³	-0.825 ^{3*}	-7.290	
	16316.320 ³	0.887 ^{3*}	1424 ¹	0.329
	16318.690 ³	-0.436 ^{3*}	-7.550	
	16324.451 ³	-0.522 ^{3*}	936 ¹	0.229
	16331.524 ³	-0.506 ^{3*}	-7.470	
	16333.141 ³	-1.356 ^{3*}	-7.450	
	16517.223 ³	0.572 ^{3*}	1414 ¹	0.329
	16612.761 ³	0.018 ^{3*}	1846 ¹	0.315
	16619.737 ³	-1.524 ^{3*}	1082 ¹	0.228
	16783.037 ³	-0.695 ^{3*}	1409 ¹	0.329
	16792.224 ³	-0.890 ^{3*}	1588 ¹	0.324
	16794.210 ³	-0.362 ^{3*}	-7.430	

Notes. a: Collisional broadening by neutral hydrogen gives either the broadening cross section $\sigma(v = 10^4\text{m/s})$ in atomic units (a_0^2), with velocity parameter α (see text for more details), or if the value is negative and no α given, then the line width is given in the standard form $\log \Gamma/N_H$ at $T = 10000$ K, where Γ is the full-width at half maximum in rad/s and N_H is in cm^{-3} . 1: BSYN based on routines from MARCS code Gustafsson et al. (2008), 2: Paul Barklem (private communication), 3: Kurucz (2014), 4: Biemont et al. (1985), *: astrophysical estimate

Table A.2: Line parameters of the lines of each element from which abundances have been derived.

Element	Wavelength (Å)	log (gf)	Broadening by H ^a	α
Mg	21059.757 ^{4*}	-0.384 ^{5*}	4440 ³	1.10
	21060.710 ^{4*}	-0.530 ⁵	4440 ³	1.10
	21060.896 ^{4*}	-1.587 ⁵	4440 ³	1.10
	21060.896 ^{4*}	-0.407 ⁵	4440 ³	1.10
	21061.095 ^{4*}	-3.383 ⁵	4440 ³	1.10
	21061.095 ^{4*}	-1.583 ⁵	4440 ³	1.10
	21061.095 ^{4*}	-0.298 ⁵	4440 ³	1.10
	21458.962 ⁶	-1.319 ⁶	4840 ³	0.359
	16434.933 ^{1*}	-1.483 ^{1*}	862 ³	0.288
Si	20804.225 ^{1*}	-1.026 ^{1*}	861 ²	0.292
	20890.415 ^{1*}	-1.613 ^{1*}	859 ²	0.292
	20926.149 ¹	-1.076 ^{1*}	1484 ²	0.324
	16150.75 ^{1*}	-0.244 ^{1*}	1872 ³	0.304
Ca	16155.244 ^{1*}	-0.674 ^{1*}	1872 ³	0.304
	16157.356 ^{1*}	-0.214 ^{1*}	1946 ³	0.284
	20962.570 ^{1*}	-0.784 ^{1*}	-7.230 ¹	
	20972.529 ¹	-1.002 ^{1*}	-7.230 ¹	
Ti	16330.532 ⁷	-0.906 ^{7*}	484 ²	0.239
	21149.625 ^{8*}	0.789 ^{8*}	-7.440	

Notes. a: Collisional broadening by neutral hydrogen gives either the broadening cross section $\sigma(v = 10^4\text{m/s})$ in atomic units (a_0^2), with velocity parameter α (see text for more details), or if the value is negative and no α given, then the line width is given in the standard form $\log \Gamma/N_H$ at $T = 10000$ K, where Γ is the full-width at half maximum in rad/s and N_H is in cm^{-3} . 1: Kurucz (2007), 2: BSYN based on routines from MARCS code Gustafsson et al. (2008), 3: Paul Barklem (private communication), 4: Brault & Noyes (1983), 5: Civiš et al. (2013), 6: manual entry by NIST lookup, 7: Lawler et al. (2013), 8: Kurucz (2016), *: astrophysical estimate

Table A.3: Spectral line data of the OH molecular lines used in the method to determine stellar parameters.

Molecule	Wavelength (Å)	log (gf)
	15236.623	-5.861
	15236.956	-5.861
	15391.057	-5.512
	15391.205	-5.512
	15469.762	-5.242
	15470.216	-5.242
	15505.324	-5.378
	15505.746	-5.378
	15651.897	-5.203
	15653.480	-5.203
	15654.112	-6.808
	16247.884	-5.177
	16312.494	-5.077
OH	16312.920	-5.077
	16346.182	-5.002
	16347.493	-5.002
	16352.213	-4.897
	16581.269	-4.874
	16714.359	-4.758
	16872.277	-5.032
	16886.275	-4.874
	16886.293	-6.976
	16895.183	-4.743
	16895.319	-5.706
	16898.778	-4.743
	16902.733	-4.674
	16909.289	-4.712

Table A.4: Spectral line data of the CN molecular lines used in the method to determine stellar parameters

Molecule	Wavelength (Å)	log (gf)
	15466.235	-1.195
	15471.812	-1.749
	15485.339	-1.779
	15489.56	-1.927
	15489.764	-1.932
	15494.748	-1.542
	15495.256	-1.196
	15496.319	-3.095
	15500.927	-1.742
	15501.498	-1.764
	15660.700	-1.521
	15661.595	-1.56
CN	15871.453	-1.633
	15881.108	-1.847
	16021.961	-1.518
	16179.943	-1.619
	16180.109	-1.131
	16329.245	-1.553
	16334.003	-1.932
	16352.092	-1.600
	16581.908	-1.215
	16582.026	-1.526
	16582.199	-1.109
	16615.321	-1.474
	16618.553	-1.891
	16791.783	-1.870
	16895.399	-1.462

Table A.5: Spectral line data of the CO molecular lines used in the method to determine stellar parameters

Molecule	Wavelength (Å)	log (gf)
	16025.53	-6.275
	16025.935	-7.004
	16026.94	-7.851
	16030.941	-6.262
	16031.274	-7.038
	16184.507	-6.26
	16184.565	-6.242
	16184.738	-6.279
	16184.912	-6.224
	16185.256	-6.298
	16185.548	-6.207
	16186.062	-6.317
	16186.473	-6.19
	16187.154	-6.337
	16187.688	-6.173
	16332.817	-5.79
	16334.087	-7.661
	16351.905	-7.148
	16352.478	-5.766
	16613.174	-5.777
	16613.225	-5.795
CO	16613.427	-5.759
	16613.579	-5.814
	16613.984	-5.742
	16614.236	-5.833
	16614.846	-5.724
	16615.195	-5.853
	16616.012	-5.708
	16616.457	-5.873
	16617.485	-5.691
	16618.021	-5.893
	16619.264	-5.675
	16619.887	-5.914
	16620.177	-7.028
	16871.668	-5.944
	16885.696	-6.849
	16895.397	-6.434
	16896.04	-5.293
	16899.304	-6.11
	16901.802	-6.527
	16902.455	-5.28
	16909.199	-5.266
	16909.543	-6.843

Table A.6

Index / Star	21059.76 Å	21060.89 Å	21458.87 Å	<[Mg/Fe]>	$\sigma[\text{Mg/Fe}] / \sqrt{N_{\text{lines}}}$
1	-0.01	0.02	0.08	0.03	0.02
2	0.03	0.06	0.09	0.06	0.01
3	0.21	0.14	0.26	0.21	0.02
4	0.07	0.02	0.08	0.06	0.01
5	-0.07	-0.04	-0.03	-0.05	0.01
6	-0.01	0.0	0.12	0.04	0.02
7	0.06	0.07	0.16	0.1	0.02
8	0.21	0.17	0.2	0.19	0.01
9	0.04	-0.01	0.07	0.04	0.02
10	0.26	0.3	0.34	0.3	0.02
11	0.01	-0.01	0.08	0.03	0.02
12	0.05	-0.0	0.1	0.05	0.02
13	-0.16	-0.08	-0.06	-0.1	0.02
14	0.07	0.05	0.14	0.09	0.02
15	-0.14	-0.12	-0.02	-0.09	0.02
16	-0.18	-0.11	-0.09	-0.13	0.02
17	0.04	0.09	0.18	0.1	0.03
18	-0.07	0.07	0.12	0.04	0.03
19	-0.06	-0.03	0.01	-0.03	0.01
20	-0.03	-0.01	0.06	0.0	0.02
21	-0.15	-0.09	-0.06	-0.1	0.02
22	-0.12	-0.01	-0.04	-0.05	0.02
23	0.08	-0.1	0.02	-0.0	0.03
24	-0.05	-0.11	-0.05	-0.07	0.01
25	-0.16	-0.2	-0.12	-0.16	0.02
26	-0.13	-0.07	-0.02	-0.08	0.02
27	-0.12	-0.1	-0.07	-0.09	0.01
28	-0.08	-0.11	-0.02	-0.07	0.02
29	0.03	0.09	0.13	0.08	0.02
30	-0.07	-0.06	0.0	-0.04	0.02
31	-0.27	-0.15	-0.11	-0.18	0.03
32	-0.12	-0.14	-0.07	-0.11	0.01
33	-0.12	-0.12	-0.06	-0.1	0.01
34	-0.01	0.0	0.03	0.01	0.01
35	-0.02	0.01	0.03	0.01	0.01
36	-0.11	-0.1	-0.05	-0.09	0.01
37	-0.12	-0.09	-0.07	-0.09	0.01
38	-0.18	-0.13	-0.06	-0.12	0.02
39	0.21	0.28	0.25	0.25	0.01
40	-0.2	-0.13	-0.14	-0.16	0.01
41	-0.18	-0.18	-0.03	-0.13	0.03
42	-0.07	-0.07	0.01	-0.04	0.02
43	-0.14	-0.12	-0.05	-0.1	0.02
44	0.2	0.19	0.3	0.23	0.02
HD132813	-0.04	-0.09	0.06	-0.03	0.03
HD175588	-0.18	-0.19	-0.01	-0.13	0.03
HD89758	-0.1	-0.13	-0.0	-0.08	0.02
HD224935	-0.12	-0.1	0.06	-0.05	0.03
HD101153	-0.11	-0.09	0.09	-0.04	0.04
HIP54396	-0.06	-0.02	0.08	0.0	0.03

Table A.7

Index / Star	16434.93 Å	20804.20 Å	20890.37 Å	20926.14 Å	<[Si/Fe]>	σ [Si/Fe] / $\sqrt{N_{lines}}$
1	0.21	0.04	0.08	0.02	0.09	0.03
2	0.06	0.05	0.1	0.06	0.07	0.0
3	0.37	0.28	0.17	0.2	0.26	0.04
4	0.18	–	–	–	0.18	0.0
5	0.06	0.06	0.09	-0.17	0.01	0.04
6	0.15	0.04	0.02	-0.0	0.05	0.02
7	0.11	–	0.06	–	0.08	0.01
8	0.26	0.34	0.06	0.34	0.25	0.04
9	0.1	0.13	0.13	0.06	0.1	0.02
10	0.38	0.29	0.36	0.36	0.35	0.01
11	0.1	0.03	-0.01	0.24	0.09	0.04
12	0.03	0.13	0.07	0.0	0.06	0.02
13	0.04	-0.07	0.05	0.0	0.01	0.02
14	0.17	0.13	0.15	-0.01	0.11	0.02
15	0.07	0.07	–	-0.13	0.0	0.04
16	0.01	-0.06	-0.0	-0.15	-0.05	0.03
17	0.22	–	0.02	–	0.12	0.05
18	0.15	0.1	–	–	0.12	0.01
19	-0.0	0.02	-0.12	-0.07	-0.04	0.02
20	-0.03	-0.02	0.13	-0.08	-0.0	0.03
21	-0.08	0.0	-0.02	-0.07	-0.04	0.02
22	-0.01	-0.08	-0.11	-0.13	-0.08	0.02
23	-0.04	-0.18	-0.08	0.22	-0.02	0.06
24	-0.14	-0.01	–	-0.06	-0.07	0.02
25	-0.08	-0.02	-0.22	-0.04	-0.09	0.03
26	-0.16	0.08	–	0.05	-0.01	0.05
27	-0.13	-0.01	-0.09	-0.0	-0.06	0.02
28	0.02	-0.05	–	-0.11	-0.05	0.02
29	0.12	0.07	0.02	0.07	0.07	0.02
30	0.01	0.04	-0.05	0.02	0.01	0.01
31	-0.06	-0.08	0.06	-0.11	-0.05	0.02
32	-0.03	0.0	-0.08	0.01	-0.02	0.02
33	-0.08	0.12	-0.12	0.08	0.0	0.05
34	-0.16	0.01	-0.0	-0.03	-0.05	0.02
35	0.04	0.03	0.0	0.0	0.02	0.0
36	0.04	-0.0	0.01	-0.02	0.01	0.01
37	0.04	0.01	0.04	-0.16	-0.02	0.03
38	-0.18	-0.03	–	-0.02	-0.08	0.03
39	0.19	0.05	0.12	0.18	0.13	0.02
40	0.04	0.06	-0.06	0.04	0.02	0.02
41	-0.14	-0.03	-0.14	-0.03	-0.09	0.03
42	-0.0	0.11	-0.01	0.01	0.03	0.02
43	-0.13	0.0	-0.11	-0.09	-0.08	0.02
44	0.45	0.24	0.34	0.28	0.33	0.04
HD132813	-0.05	0.07	–	–	0.01	0.03
HD175588	-0.09	-0.0	0.12	-0.07	-0.01	0.04
HD89758	0.1	0.01	-0.04	-0.01	0.02	0.02
HD224935	-0.05	-0.11	0.01	0.06	-0.02	0.03
HD101153	-0.02	-0.02	0.04	0.01	0.0	0.01
HIP54396	-0.14	0.03	0.09	–	-0.01	0.05

Table A.8

Index / Star	16136.82 Å	16150.76 Å	16155.24 Å	16157.36 Å	20962.57 Å	20972.53 Å	<[Ca/Fe]>	$\sigma[\text{Ca/Fe}] / \sqrt{N_{\text{lines}}}$
1	-0.03	-0.01	0.09	0.01	0.07	0.09	0.04	0.02
2	-0.02	0.05	0.07	0.08	0.05	0.07	0.05	0.01
3	0.14	0.14	0.18	0.11	0.16	0.19	0.15	0.01
4	-0.13	-0.0	-0.02	-0.04	0.01	-0.08	-0.04	0.02
5	-0.22	-0.18	0.0	-0.13	-0.01	-0.08	-0.1	0.04
6	-0.07	0.01	0.04	-0.0	0.06	0.04	0.01	0.01
7	0.09	0.06	0.13	0.01	0.17	0.21	0.11	0.02
8	0.02	0.05	0.14	0.04	0.22	0.17	0.11	0.03
9	0.02	-0.04	0.1	-0.02	0.1	0.07	0.04	0.02
10	0.26	0.22	0.24	0.19	0.21	0.32	0.24	0.01
11	0.01	0.04	0.08	0.01	0.03	0.13	0.05	0.02
12	0.02	0.06	0.09	0.01	0.09	0.07	0.06	0.02
13	-0.05	-0.01	0.07	-0.01	0.08	0.09	0.03	0.02
14	0.01	0.0	0.1	0.02	0.11	0.11	0.06	0.02
15	-0.04	-0.0	0.09	0.01	0.09	0.08	0.04	0.02
16	-0.23	-0.18	-0.11	-0.17	-0.06	-0.09	-0.14	0.02
17	0.05	-0.03	0.04	0.04	0.13	0.03	0.04	0.01
18	-0.05	-0.01	0.03	-0.0	0.03	0.05	0.01	0.01
19	-0.14	-0.09	0.04	-0.03	-0.0	0.06	-0.03	0.03
20	-0.07	-0.01	0.1	0.02	0.12	0.1	0.04	0.03
21	-0.06	-0.02	0.12	-0.02	0.11	0.11	0.04	0.03
22	-0.15	-0.1	0.04	-0.06	0.07	0.08	-0.02	0.04
23	-0.1	0.13	0.02	0.0	0.01	0.02	0.01	0.01
24	-0.07	-0.06	0.03	-0.04	-0.02	0.03	-0.02	0.02
25	-0.07	0.04	0.09	-0.04	0.09	0.04	0.02	0.03
26	-0.08	-0.05	0.01	-0.01	0.06	0.07	0.0	0.02
27	-0.11	-0.04	0.04	-0.07	0.05	0.02	-0.02	0.02
28	-0.09	-0.02	0.04	-0.05	0.07	0.13	0.01	0.03
29	-0.21	-0.17	-0.02	-0.08	0.01	-0.0	-0.08	0.04
30	-0.06	-0.12	0.05	-0.02	0.09	0.12	0.01	0.03
31	-0.18	-0.11	-0.0	-0.14	0.02	0.04	-0.06	0.04
32	-0.1	-0.06	0.03	-0.05	0.03	0.05	-0.02	0.02
33	-0.12	-0.01	0.07	-0.05	0.02	0.05	-0.01	0.02
34	-0.07	-0.0	0.12	0.02	0.11	0.15	0.06	0.03
35	-0.09	-0.04	0.08	-0.01	0.08	0.11	0.02	0.03
36	-0.01	0.0	0.12	-0.03	0.06	0.16	0.05	0.03
37	-0.16	-0.12	0.0	-0.09	0.0	0.01	-0.06	0.03
38	-0.16	-0.12	-0.06	-0.12	0.03	0.03	-0.07	0.03
39	0.12	0.07	0.19	0.14	0.24	0.17	0.16	0.02
40	-0.13	-0.12	0.02	-0.15	0.01	0.09	-0.05	0.03
41	-0.04	0.05	0.17	0.02	0.08	0.14	0.07	0.03
42	0.01	0.02	0.12	-0.0	0.05	0.12	0.05	0.02
43	-0.04	-0.0	0.1	-0.01	0.07	0.1	0.04	0.02
44	0.21	0.16	0.24	0.14	0.26	0.27	0.21	0.02
HD132813	-0.03	-0.02	0.02	-0.1	0.12	0.19	0.03	0.04
HD175588	-0.06	-0.03	0.07	-0.1	0.13	0.18	0.03	0.04
HD89758	-0.1	-0.08	0.06	-0.06	0.09	0.04	-0.01	0.03
HD224935	-0.11	-0.07	0.04	-0.1	–	0.12	-0.02	0.04
HD101153	-0.14	-0.06	0.02	-0.15	–	0.13	-0.04	0.04
HIP54396	-0.11	-0.05	0.03	-0.09	0.13	0.13	0.01	0.04

Table A.9

Index / Star	16330.54 Å	21149.62 Å	<[Ti/Fe]>	σ [Ti/Fe] / $\sqrt{N_{lines}}$
1	0.08	0.11	0.1	0.01
2	0.01	0.32	0.17	0.07
3	0.2	0.31	0.25	0.03
4	0.04	0.04	0.04	0.0
5	-0.08	0.07	-0.01	0.04
6	0.07	–	0.07	0.0
7	0.13	0.31	0.22	0.04
8	0.22	0.38	0.3	0.04
9	0.09	-0.03	0.03	0.03
10	0.36	0.43	0.39	0.01
11	0.1	0.21	0.16	0.03
12	0.08	0.2	0.14	0.03
13	0.02	0.23	0.12	0.05
14	0.12	0.34	0.23	0.05
15	-0.03	0.23	0.1	0.06
16	-0.1	0.01	-0.04	0.03
17	0.04	0.06	0.05	0.01
18	0.08	0.08	0.08	0.0
19	0.01	0.01	0.01	0.0
20	0.0	0.03	0.02	0.01
21	0.0	0.02	0.01	0.01
22	-0.09	0.1	0.01	0.04
23	-0.04	-0.05	-0.05	0.0
24	-0.05	0.08	0.01	0.03
25	-0.0	0.11	0.05	0.03
26	0.12	-0.03	0.04	0.04
27	-0.0	0.09	0.04	0.02
28	-0.01	0.08	0.03	0.02
29	-0.06	0.12	0.03	0.04
30	0.01	0.05	0.03	0.01
31	-0.12	-0.03	-0.08	0.02
32	0.02	0.02	0.02	0.0
33	-0.01	0.06	0.02	0.01
34	0.01	0.0	0.0	0.0
35	0.04	0.09	0.07	0.01
36	0.02	0.08	0.05	0.01
37	-0.08	0.03	-0.02	0.03
38	-0.06	-0.02	-0.04	0.01
39	0.14	0.26	0.2	0.03
40	-0.11	0.01	-0.05	0.03
41	-0.02	0.12	0.05	0.04
42	-0.02	0.04	0.01	0.01
43	-0.02	0.05	0.01	0.01
44	0.28	0.37	0.32	0.02
HD132813	0.0	0.24	0.12	0.06
HD175588	-0.05	0.2	0.07	0.06
HD89758	-0.07	0.2	0.06	0.06
HD224935	-0.01	0.26	0.12	0.06
HD101153	-0.08	0.16	0.04	0.06
HIP54396	-0.02	0.12	0.05	0.03

Table A.10: Uncertainties in the derived Mg, Si, Ca and Ti abundances from each individual line arising from typical uncertainties of ± 100 K in T_{eff} , ± 0.2 dex in $\log g$, ± 0.1 dex in $[\text{Fe}/\text{H}]$, and ± 0.1 km/s in ξ_{micro} . We have selected seven stars with metallicities covering the range explored in this study (metallicities are mentioned in brackets below the name of each star). The abundance uncertainty, i.e. dispersion estimated from the gaussian fit to the distribution of 50 abundance estimates (estimated using 50 sets of stellar parameters) from each line is listed in each column. The mean uncertainty based on error propagation is listed in the row after each element.

	Index	10	44	11	30	29	41	40
	[Fe/H]	-0.9 dex	-0.6 dex	-0.5 dex	-0.25 dex	0.0 dex	0.1 dex	0.25 dex
	λ (\AA)	σ_{line}	σ_{line}	σ_{line}	σ_{line}	σ_{line}	σ_{line}	σ_{line}
[Mg/Fe]	21059.76	0.10	0.08	0.10	0.08	0.09	0.11	0.12
	21060.89	0.12	0.12	0.14	0.07	0.13	0.13	0.13
	21458.87	0.10	0.10	0.10	0.10	0.11	0.12	0.14
$\sqrt{\sum \sigma_{\text{line}}^2} / N_{\text{lines}}$		0.04	0.04	0.07	0.05	0.07	0.07	0.08
[Si/Fe]	16434.93	0.2	0.33	0.28	0.27	0.34	0.30	0.36
	20804.20	0.13	0.12	0.14	0.15	0.15	0.15	0.13
	20890.37	0.11	0.07	0.12	0.10	0.13	0.11	0.13
	20926.14	0.13	0.10	0.14	0.15	0.16	0.11	0.17
$\sqrt{\sum \sigma_{\text{line}}^2} / N_{\text{lines}}$		0.07	0.09	0.09	0.09	0.11	0.09	0.11
[Ca/Fe]	16150.76	0.14	0.18	0.12	0.21	0.16	0.25	0.09
	16155.24	0.10	0.10	0.08	0.14	0.12	0.13	0.06
	16157.36	0.14	0.10	0.09	0.14	0.10	0.13	0.12
	20962.57	0.09	0.08	0.07	0.11	0.08	0.10	0.10
	20972.53	0.12	0.06	0.10	0.12	0.11	0.09	0.09
$\sqrt{\sum \sigma_{\text{line}}^2} / N_{\text{lines}}$		0.05	0.05	0.04	0.07	0.05	0.07	0.05
[Ti/Fe]	16330.54	0.14	0.14	0.09	0.19	0.14	0.20	0.08
	21149.62	0.17	0.15	0.11	0.12	0.09	0.09	0.10
$\sqrt{\sum \sigma_{\text{line}}^2} / N_{\text{lines}}$		0.11	0.10	0.07	0.11	0.08	0.11	0.06